HIGH-RESOLUTION ANALYSIS OF HYPERGLYCEMIC BONE QUALITY DURING THE EARLY STAGES OF BONE FORMATION

By

Emily-Rose Creighton

A Thesis Submitted to the School of Graduate Studies in Partial Fulfillment of the Requirements for the Degree Master of Applied Science

MASTER OF APPLIED SCIENCE (2016), School of Biomedical Engineering

McMaster University, Hamilton, Ontario

Title: Investigating hyperglycemic bone formation with high resolution microscopy techniques

Author: Emily Rose Creighton

Supervisor: Dr. Kathryn Grandfield

Number of pages: xx, 82

LAY ABSTRACT

According to the International Diabetes Federation, 387 million people worldwide are living with diabetes of which 46.3% are undiagnosed. Uncontrolled diabetes results in hyperglycemia, which is a condition where there is an increased level of glucose in the blood. When diabetes is not regulated correctly with medication, it leads to problems in the long-term success rate of dental implants. The objective of this thesis was to investigate the early stages of bone formation, which are accepted to be critical in the long-term success rate of dental implants, in hyperglycemic animal models compared to control groups using various microscopy techniques. The different techniques used allowed for the structural and elemental compositions of bone to be studied on the micro-scale and nano-scale. It was shown that at the 5-day healing time point studied, the micro-structure, rather than the nano-structure, was negatively altered in the hyperglycemic group compared to the control group.

ABSTRACT

Consensus in scientific literature is that hyperglycemia, which is a condition that manifests in individuals with uncontrolled diabetes, causes compromised bone growth, but the exact mechanisms of are unknown. It has been estimated that 5% of dental implant failures that have previously been linked to unknown causes may be associated with undiagnosed diabetes. It is important to study the early stages of bone growth as it is accepted that they are critical in the long-term success rate of endosseous implants. This study aimed to investigate the bone healing seen in the hyperglycemic group compared to the normal (i.e. control) group, at an early time point, using high-resolution microscopy techniques.

Ten young (200-250gram) male Wistar rats were used for this study with five rats assigned to the control group and the other five rats intravenously injected with 65 mg/kg of streptozotocin (STZ) to induce diabetes. An osteotomy model was used to make a 1.3mm defect in the diaphysis of the rat femurs. After five days, the femurs were removed, fixed in glutaraldehyde, dehydrated, and embedded in resin. Structural and chemical analyses were conducted on the samples using a variety of microscopy techniques to examine various factors of bone quality including: bone porosity, relative mineralization level, and the arrangement of collagen and mineral.

When analyzing the micro-structure, the hyperglycemic group showed increased porosity in the newly formed bone as compared to the control group. However, no significant differences were found in the nano-structure when analyzing the arrangement of collagen and mineral.Therefore, the results in this thesis suggest that alterations in micro-architecture rather than nano-architecture may play a pivotal role in the compromised bone healing in uncontrolled diabetes at this five-day time point. Future work should investigate additional time points in the bone healing process.

ACKNOWLEDGMENTS

First and foremost I would like to thank Dr. Kathryn Grandfield for providing me with this wonderful opportunity and invaluable knowledge. I am forever grateful for her consistent guidance and support. She has been a wonderful mentor and role model making this journey exceptional for me. Next, I would like to thank the members of Grandfield Research Group (GRG) who have had an active role in helping me with this project including: Vicky Vuong for all her SEM help, James Tedesco for his micro-CT help, and Bryan Lee for his statistical knowledge. I would also like to thank other the members of GRG who have been along for the ride with me including: Dakota Binkley, Daniel Osorio, and Xiaoyue Wang. I could not have asked for a more generous, thoughtful, and fun research group. Thank you for the countless hours you listened and critiqued both my presentations and research. I would also like to thank our collaborator Dr. John Davies and his students, Dillon Caines and Robert Liddell, who helped make this project possible. Thank you for all the sample preparation and feedback your laboratory group provided throughout the project.

Next I would like to thank some McMaster staff and Post-Doctorate Students including the following: Steven Kornic (for Raman spectroscopy guidance), Marcia Reid (for sample preparation and TEM teaching), Carmen Andrei (for SAED, EDS, and EELS results), and David Rossouw (for image processing knowledge). Thank you for your patience, time, and knowledge. I would also like to thank the institutions who provided the microscopes, which were used in this thesis, including the following facilities: Canadian Centre of Electron Microscopy, Electron Microscopy Facility in the Health Science Centre at McMaster University, McMaster University Automotive Resource Centre, and Department of Chemistry at McMaster University.

I would also like to thank my boyfriend, David Joyal, for consistently listening to my all my minor life dramas and making me smile every day throughout this past year and a half. Also, last but not least I would like to thank my family: Susan, Bruce, and Brendon Creighton for everything you have done for me. This thesis is a small chapter in my life and I would not have made it to where I am today without all of you.

TABLE OF CONTENTS

LIST OF FIGURES

LIST OF TABLES

LIST OF ABBREIVATIONS

ACP: amorphous calcium phosphate

AGEs: advanced glycation end-products

BIC: bone-implant contact

BF: bright-field

BMD: bone mineral density

BSE: backscattered electron

Ca/P Ratio: calcium to phosphorous ratio

CB: cortical bone

CF: collagen fibrils

DF: dark-field

DMB: degree of mineralization of bone

D-spacing: D-periodic spacing

ECM: extracellular matrix

EDS: energy dispersive x-ray spectroscopy

EELS: electron energy loss spectrometry

FIB: focused ion beam

HA: hydroxyapatite

HAADF: high angle annular dark field

IGF: insulin-like growth factor

MF: mineralized front

MI: mineralized islands

Micro-CT: micro-computed tomography

MSCs: mesenchymal stem cells

NB: newly formed bone

TEM: transmission electron microscopy

T1DM: type 1 diabetes mellitus

T2DM: type 2 diabetes mellitus

ROI: region of interest

SAED: selected area electron diffraction

SE: secondary electron

SEM: scanning electron microscopy

STEM: scanning transmission electron microscopy

STZ: streptozotocin

DECLARATION OF ACADEMIC ACHIEVEMENT

I hereby declare that the contents in this thesis were written by myself and that the appropriate citations and acknowledgements have been given. All animal experiments were conducted by our collaborators at the University of Toronto. The samples were fixed, dehydrated, and embedded at the University of Toronto and delivered to me at McMaster University for the characterization developed and reported in this thesis. For the bone porosity section of this thesis, I performed all the image processing and calculations for the 2D and 3D results. I acquired the majority of the SEM images (8 out of 10 of the samples) used for porosity calculations (not shown in this thesis, but used for calculations). Vicky Vuong assisted with SEM imaging during my training, and as such, she assisted in the recording of some of the images presented herein. I polished the samples for SEM and the gold coating was done by technicians at the CCEM. Two out of four of the micro-CT acquisitions were done James Tedesco and the other two I acquired. I performed all the 2D reconstruction and 3D modelling for the micro-CT images using the software programs mentioned in the thesis. For the bone relative mineralization section, I conducted all of the Raman spectroscopy data acquisitions and processing. For the collagen-mineral arrangement section of this thesis, the ultramicrotome sectioning and staining for TEM preparation was done at the Electron Microscopy Facility in the Health Science Centre at McMaster University. Focused Ion Beam preparation and carbon coating of samples were done by technicians at the CCEM and the image acquisition done on the JEOL 2010 with the SAED, EDS, and EELS were also done by technicians at the CCEM with my guidance on ROI selection. The HAADF-STEM images from the Titan 80-300LB were acquired with the help of my supervisor. I acquired the all the TEM images from the JEM 1200EX TEMSCAN shown in this thesis (along with others used for the collagen fibril measurements). I also did all the collagen fibril diameter and D-spacing measurement using image processing software and calculated the Ca:P ratios.

CHAPTER 1

INTRODUCTION

1.1 BONE BACKGROUND

1.1.1 BONE TISSUE: MACRO-STRUCTURE AND MICRO-STRUCTURE

Bone is a complex and hierarchical structure (Figure 1.1) that contributes to a number of important physiological functions such as skeletal support, organ protection, movement, blood cell production, immune response, as well as providing a mineral and energy storage site [10] . The five types of bones in the body are long bones, short bones, flat bones, irregular bones, and sesamoid bones [10]. The two types of osseous tissues that form these bones are cortical bone (compact bone) and trabecular bone (cancellous bone). In general, an adult human skeleton is composed of approximately 80% cortical bone and 20% trabecular bone. However, different anatomical regions have different ratios. For example, the ratio of cortical to trabecular bone in the femoral head is 50:50 and the ratio in radial diaphysis is 95:5. The macro-structures of cortical and trabecular bone are vastly different, with trabecular bone resembling a honey-comb network while cortical bone consists of a denser structure which surrounds the trabecular bone [11]. Bone porosity also varies significantly depending on bone type and anatomical location. Cortical bone porosity ranges from 5-10% and trabecular bone porosity ranges from 50-90%, which is filled mainly with bone marrow [12].

On the micro-scale, the mature bone in the human skeleton is lamellar bone. Lamellar bone is composed of bone lamellae, organized arrays of mineralized collagen fibrils [13]. The immature form of bone, which will be replaced by lamellar bone, is referred to as woven bone. Woven bone consists of disorganized mineralized collagen fibrils and is present during fetal development and during the bone healing process [12].

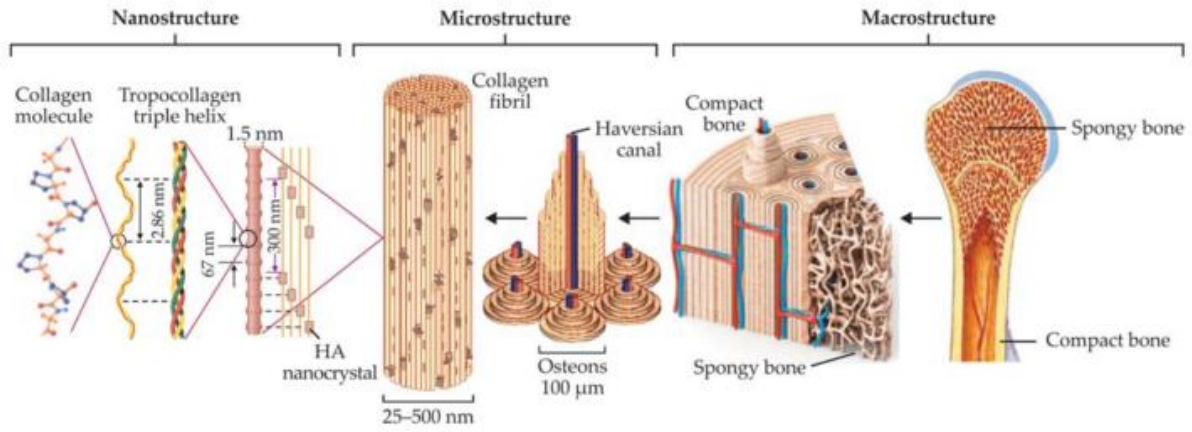

Figure 1.1 Bone Hierarchical Structures. The nanostructure is made up mainly of collagen molecules and hydroxyapatite (HA), the microstructure is made up of organized collagen fibers, and the macrostructure is made up of cortical (compact) and trabecular (spongy) bone. Adapted and with permission of use from [1]**.**

Bone quality, the ability of bone to resist fractures, is dependent on both the geometrical factors, such as the macro- and micro-architectural structures, and the material composition of bone [14], [15]. Bone disease, such as osteoporosis, can detrimentally alter these architectural structures causing a decrease in bone quality, and ultimately one's health [15], [16]. Diabetes, a metabolic disease, is also hypothesized to contribute to abnormal micro-architectural structure and/or abnormal material composition that causes a reduction in bone quality [17].

1.1.2 BONE TISSUE: NANO-STRUCTURE

In addition to the significant research on the macro- and micro-structure of bone that has been conducted, newer advanced high-resolution microscopy techniques have more recently made it possible to analyze the nano-structure of bone. Studies have suggested that while the ultrastructure of bone appears to be similar for all organisms with an internal skeleton, the exact nano-structural features are not well known [4], [5]. It is believed that variations in the nano-structure might have an adverse effect on bone quality in diseased states, such as in diabetes [7], [18].

On the nanoscale, the organic and inorganic portions of bone are predominantly Type 1 collagen fibrils and hydroxyapatite (HA), which are responsible for the tensile and compressive properties of bone, respectively [12]. The extracellular matrix (ECM), also known as bone matrix, is the extracellular portion of the bone, which is unique among connective tissue in that it can be mineralized [19]. Before the ECM is mineralized it is referred to as osteoid [20]. Mineralized ECM is composed of approximately 60% inorganic material, 30% organic material, and 10% water [4].

Collagen is a hierarchical structure which comprises the majority of the organic component of bone. Other organic components of bone include proteoglycans, matrix proteins, and growth factors [11]. Structurally, triple helical collagen molecules form collagen fibrils, which aggregate together to form collagen fibers [19]. Collagen fibrils have a characteristic banding pattern with a periodicity of 67nm, referred to as D-periodic spacing (D-spacing). This 67nm can be divided into a gap zone (40nm) and an overlap zone (27nm) where the gap zone reside between ends of the co-aligned collagen fibrils [4] (Figure 1.2).

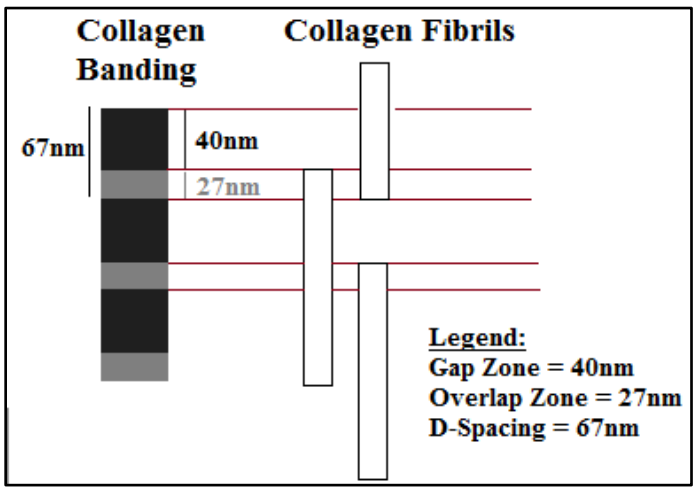

Figure 1.2 Collagen Fibril Structure. Collagen fibrils are composed of an overlap region, 27nm, and a gap region, 40nm. Based on Figure from [2].

The mineral structures in bone are considered to be polycrystalline bioapatite, commonly referred to as HA crystals with the chemical formula $Ca_{10}(PO_4)_6(OH)_2$. These polycrystalline mineral structures are platelet-like structures approximately 5nm thick, 70nm wide and on the order of 100nm long [4]. Common ionic substitutions in bioapatite are the replacement of the anion PO_4^{-3} by CO_3^{-2} and HPO_4^{-2}, to form carbonate apatite and HPO_4^{-2} bearing apatite, respectively [21], [22].

1.1.3 BONE TISSUE: COLLAGEN-MINERAL ARRANGEMENT

There is currently debate regarding the exact nanoscale arrangement of collagen and mineral in lamellar bone. Hodge and Petruska first proposed the model that the mineral lays within the gap regions without disrupting the fibrillar structure [23]. This model is referred to as intrafibrillar mineralization and is the theory that is most predominately accepted (Figure 1.3A). However, recent research has demonstrated that these gap regions may not contain all of the mineral [24]. These studies have shown the total amount of mineral in the bone structure is significantly more than the total amount of mineral that can be confined solely to the gap zones and propose that this mineral extends pass the gap zones into regions between the collagen fibril, referred to as interfibrillar mineralization [4], [25] (Figure 1.3B). The term extrafibrillar material has been used in literature to describe irregularly shaped fragments seen in high-resolution microscopy imaging [26]. Sometimes the term extrafibrillar mineralization is also interchanged with the term interfibrillar mineralization [27]. However, extrafibrillar mineralization generally refers to the mineralization that does not appear to be guided by the collagen fibrils [8].

It has been speculated that interactions between collagen fibrils and mineral crystals may be different in diseased states of bone than healthy bone [18]. These alterations include differences in mineralization levels, which are thought to alter collagen fibril diameter and D-spacing. In

particular, a study done on collagen fibrils in rat tendons illustrated that less mineralized collagen fibrils may have a smaller diameter and a larger D-spacing than more mineralized collagen fibrils [28].

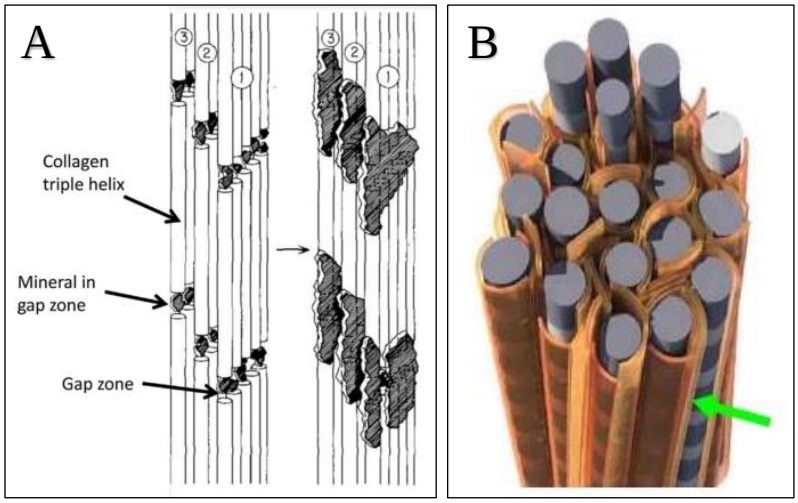

Figure 1.3 Mineralization Patterns. A) The process of mineralization where intrafibrillar mineralization (where the mineral lies within the gap zones of the collagen fibril) occurs and then the extra mineral (which cannot be account for in the gap zones) extend between the collagen fibrils, interfibrillar mineralization. Adapted and with permission of use from [3]. B) A schematic of complete interfibrillar mineralization, where the mineral lies between adjacent collagen fibrils, with permission of use from [4].

1.1.4 OSSIFICATION AND BONE REMODELLING

Bone is a dynamic organ in that it is constantly being remodelled throughout an organism's lifespan to adapt to changing environments and repair damage. Ossification, the process of bone formation, occurs through intramembranous ossification or endochondral ossification [29], [30]. During intramembranous ossification, mesenchymal stem cells (MSCs) will aggregate and differentiate into osteoblasts. The osteoblasts are responsible for laying down the organic matrix, referred to as osteoid. Subsequently, an inorganic layer of HA is deposited onto the osteoid through a process called mineralization [29]. Endochondral ossification is a similar process to intramembranous ossification except during endochondral ossification an intermediate cartilage

layer exists. During endochondral ossification, the aggregation of MSCs will lead to the differentiation and hypertrophic growth of chondrocytes that form the cartilage layer. The cartilage layer is eventually removed and replaced by osteoblasts, which secrete the appropriate factors that produce organic and inorganic matrix [29].

Bone remodelling, on the other hand, involves the coupling of both bone formation and bone resorption by the respective cell types, osteoblasts and osteoclasts. When osteoid becomes mineralized during bone formation, osteoblasts get trapped in the mineralized matrix to become osteocytes. Osteocytes, which reside in the lacuna of mineralized bone have mechanotransduction mechanisms that allows them to convert mechanical strain to biochemical signals to control the remodelling process in response to environmental stimuli [31]. During bone resorption, the osteoclasts release acidic compounds that first degrade the inorganic matrix, followed by secretion of enzymes that are responsible for digesting the organic layer [1]. This dynamic remodelling process is important in maintaining good bone quality and disruption of this remodelling process is speculated to be an issue in diseases including diabetes [32].

1.1.5 WOUND HEALING AND WOVEN BONE STRUCTURE

Bone healing is unique, compared to other soft-tissue healing process, since bone can regenerate without the formation of scar tissue [33]. The healing process is influenced by several different factors including the type of bone tissue, anatomical location, and the level of trauma sustained to the tissue [34]. Multiple factors include infection, stress, and diabetes can interfere with the healing process leading to impaired wound healing [35], [36]. First a hematoma, or blood clot, will form at the site of injury. Once the hematoma is fully formed, specific cells known as neutrophils and monocytes remove it within a few days via phagocytosis. Then angiogenesis, the development of new blood vessels, occurs and migratory osteogenic cells move to target locations

to secrete osteoid, which then becomes mineralized in order to form woven bone. The woven bone will then be replaced by lamellar bone through the previously mentioned remodelling process [34], [37], [38].

There is still debate regarding the exact biomineralization process in early bone formation [39], as it is difficult to study *in-vivo* biomineralization at the nano-scale [8]. Despite this obstacle, current literature proposes that collagen fibrils and/or matrix vesicles act as nucleation sites for apatite crystal formation [8], [40], [41]. Similar to lamellar bone, woven bone has platelet-shaped apatite crystals; however, HA crystals appear to be smaller in woven bone than in lamellar bone, which may be due to the rapid deposition of woven bone [5]. Originally, it was proposed that, during early stages of mineralization, collagen fibrils were the sole sites of mineralization, and that the mineral was localized within the characteristic periodicity banding pattern [42]. In particular, it was hypothesized that specific atomic interactions in the gap zones of these collagen fibrils initiate calcification [43]. However, electron microscopy studies have shown aggregates of mineralized clusters not associated with the collagen fibrils [39]. It is believed that the initial calcification locations for these aggregates arise from the matrix vesicles (ranging from 0.05 to 0.45μm) that bud off from cell membranes; the lipids within these vesicles lead to liquid-calcium interactions, which facilitates these calcification loci [44]. These aggregates are referred to as calcification nodules (ranging from 0.5μm to 1.5μm), also known as calcospherites or mineralized nodules [8], [41], [45], [46] (Figure 1.4A). It is suggested that these aggregates which arise from the matrix then spread through the surrounding matrix and come into contact with collagen fibrils [39]. When nodules agglomerate they become referred to as mineralized islands (or calcification islands) [39], [45]. As the collagen fibrils become more closely packed during the bone formation,

a more apparent crystal orientation, with the c-axis of the crystals aligning with the long axis of the collagen fibrils, is noted [5], [41] (Figure 1.4B).

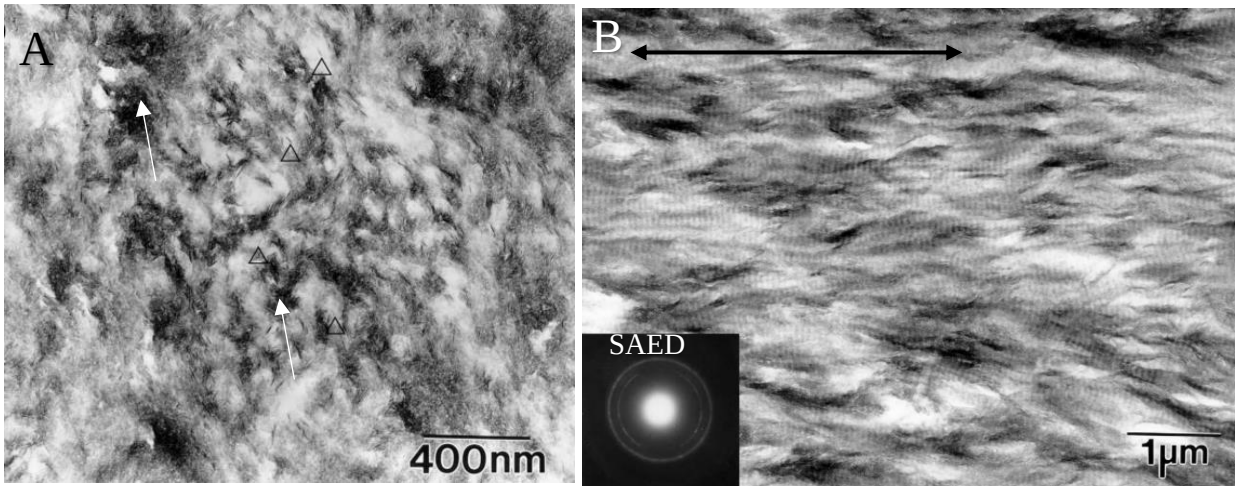

Figure 1.4 Newly Formed Bone. A) Transmission electron microscope (TEM) image of the collagen fibrils from the diaphysis of a 21-week-old human fetus with white arrows pointing to structures that resemble mineralized islands. Adapted and with permission of use from [5]. B) TEM image of a mid-diaphysis femur from 19-week old human fetus with a corresponding selected area electron diffraction (SAED), showing a preferred (002) crystallographic orientation with the long axis of the collagen fibrils (i.e. in the direction of the double pointed arrow), with permission of use from [5].

1.2 DIABETES MELLITUS

1.2.1 GLUCOSE REGULATION

The pancreas is comprised of pancreatic islet cells, which regulate glucose homeostasis. The three main types of cells composing the pancreatic islet are insulin-producing beta cells, glucagon-releasing alpha cells, and somatostatin-producing gamma cells. Regulated insulin production prevents hyperglycemia, a condition where there is increased glucose levels in the blood, by allowing cells to uptake glucose for energy and by storing glucose in the liver in the form of glycogen. Glucagon acts in opposition to insulin by breaking down glycogen into glucose,

therefore increasing blood glucose levels. Lastly, somatostatin inhibits insulin and glucagon secretion [47].

1.2.2 TYPES OF DIABETES

According to the International Diabetes Federation, 387 million people worldwide are currently living with diabetes and of which 46.3% are undiagnosed [48]. People with uncontrolled diabetes suffer from hyperglycemia [49]. The two main types of diabetes are type 1 diabetes mellitus (T1DM) and type 2 diabetes mellitus (T2DM), which are responsible for approximately 5-10% and 90-95% of the diabetic population, respectively [50]. The third type of diabetes which is less common is gestational diabetes, which occurs during pregnancy [51]. T1DM is an autoimmune condition where the immune system destroys the beta cells of the pancreas, leading to a substantial reduction in insulin production [16]. T2DM is caused when cells become resistant to the uptake of glucose through specific channels in the cell membrane. The onset factors differ between the two types of diabetes as T1DM tends to be the result of genetic factors, whereas T2DM is primarily recognized to be caused by environmental factors including lack of exercise and high sugar diets, however genetic factors may still be a contributing factor to T2DM [49].

1.2.3 BONE QUALITY IN DIABETES

Research has shown that individuals with T1DM generally have reduced bone mineral density (BMD) and lower bone mass than non-diabetic individuals [52], [53]. However, those who suffer from T2DM do not necessary have a reduced bone mass compared to non-diabetic individuals [49]. Research on T2DM has been inconsistent as studies have shown both increased levels and normal levels of BMD [54], [55]. The inconsistency in BMD levels when examining diabetes may be due to differences in the anatomical region, the type of bone, or the type and age of the animal model used [49].

Regardless of the inconsistent results in bone mass or BMD, both T1DM and T2DM individuals tend to have increased fracture rates [56], [57]. Therefore, it is suggested that diabetes is associated with reduced bone quality rather than solely reduced bone mass or BMD [55]. Bone quality can be influenced by the size, the shape, the microarchitecture, and both the collagen and mineral components of bone [14]. As such, investigating the elemental composition and structural organization of the bone may help explain why diabetics are more prone to fractures compared to non-diabetic individuals despite varying opinions on diabetic BMD in literature [56].

Bone porosity is an important factor in bone quality. In general, increased porosity is correlated with poor bone quality [58]. Altered bone turnover rates might be responsible for these adverse changes in porosity [17]. Research has shown that those with diabetes have an increased cortical bone porosity, which is indicative of decreased bone quality [58]–[60]. However, other research suggests that there is a lack of significant structural abnormalities between diabetic and non-diabetic individuals [61], [62].

An important indicator of bone strength is the degree of mineralization of bone (DMB), also commonly referred to as mineral to matrix ratio, which is regulated by the bone remodelling rate. The DMB distribution is heterogeneous due to the varying amounts of mineral deposition at sites of bone growth. It is suggested a lower bone turnover, with a constant speed of mineralization, will increase the DMB and decrease its heterogeneity, whereas an increase bone turnover will decrease DMB and increase its heterogeneity [63]. Research on diabetic bone has shown contradicting results illustrating both decreased mean DMB and increased mean DMB presumably due to abnormal bone turnover rates [64][65]. While the exact differences in the bone cellular activities regulating bone turnover in hyperglycemic individuals are not fully understood, it has been suggested that diabetes reduces osteoblast activity, as it has been shown that insulin is

important in osteoblast formation [57], [66]. The effect of diabetes on osteoclast formation and activation is controversial in literature with some research reporting increased osteoclastic activity [20], other research reporting little change in osteoclastic activity [57], and yet others reporting decreased osteoclast numbers [67].

Another important parameter in bone quality is the quality of the mineral present. The mineral quality is dependent on crystallinity, maturity, and level of ionic substitution in the apatite structure [63]. Research on diabetes has suggested that there is a decreased crystal size compared to control groups which could be due to decreased bone turnover. However, there does not appear to be a difference between metabolic groups in the calcium to phosphorous ratio (Ca/P ratio), which has been correlated to crystal maturity levels, with a lower Ca/P ratio indicating less mature bone [68].

Collagen morphology is also important in bone quality. For example, the mechanical strength of collagen is influenced by enzymatic and non-enzymatic cross-link formation between adjacent collagen molecules. Enzymatic cross-linking is believed to increase bone quality by reducing collagen slips, which is believed to be important in toughening bone [13]. Advanced glycation end-products (AGEs) have adverse effects on bone quality. They inhibit enzymatic cross-links, which are beneficial to bone quality. This can lead to stiffening of the collagen matrix, which may alter collagen morphology [19]. These products can form in bone when glucose reacts with collagen. Disrupted enzymatic cross-linking and/or increased non-enzymatic cross-linking have been shown to reduce bone quality in diabetic patients [13].

1.2.4 WOUND HEALING IN DIABETES

In addition to increased fracture rates, presumably due to reduced bone quality, research consistently shows delayed wound healing, delayed osseous healing, and increased implant failure

rates in diabetic groups [57], [69], [70]. According to the American Diabetes Association 2008 report, 25% of diabetic individuals will suffer from wound problems [71]. Therefore, it is important to look at the early stages of bone formation in diabetic individuals and the interaction between newly formed bone and the implant [50].

Impaired wound healing in diabetes has been attributed to a number of factors including decreased or impaired growth factor production (such as insulin-like growth factor, IGF), angiogenic response, macrophage function, and fibroblast (cells responsible for ECM and collagen formation) migration and proliferation [71], [72]. For example, in hyperglycemic induced animal models, a 10-fold decrease in IGF expression has been observed after five days of wound healing [71].

Osseous healing, both intramembranous and endochondral ossification, is also disrupted by diabetes [36]. Diabetic animals, compared to control groups show impaired osteoid matrix production, reduced MSC differentiation into osteoblasts, impaired osteoblastic proliferation, and decreased osteoblastic activity in the critical early stages of bone healing [16], [36], [73]. However, it has been shown that when diabetes is under control with the treatment of insulin, glucose uptake, bone turnover rate, osteoblast proliferation, and collagen production are returned back to normal physiological levels [73]. This suggests that insulin has an anabolic role in bone healing and without proper regulation of insulin bone healing is impaired [74].

1.2.5 IMPLANT FAILURES

A functional connection between artificial devices, such as dental implants, and native bone, termed osseointegration, must be established at the bone-implant interface in order for implanted devices to perform their desired functions. Advances in dental implant designs over the years have substantially improved implant success rates. Studies have shown survival rates for

dental implant in humans between 85-95% [75], [76]. However, it has been estimated that approximately 5% of dental failures are due to poorly controlled or misdiagnosed diabetes [69].

Implants in diabetic individuals show poor osseoconduction, the ability of bone to grow along the implant surface, which is believed to be caused by delayed hematoma formation and depleted levels of signalling molecules essential in osseoconduction [69], [77]. When hyperglycemia is under control in diabetic patients, implant failure is less prevalent. However, many individuals are unaware that they suffer from diabetes, and therefore hyperglycemia [78]. With a better understanding of how diabetes affects bone healing at the micro- and nano-scale level, a preventative implant design can potentially be invented to increase implant success rates for undiagnosed and uncontrolled diabetic individuals.

1.3 RESEARCH MOTIVATIONS AND OBJECTIVES

Consensus in scientific literature is that uncontrolled or misdiagnosed diabetes, in which hyperglycemia is present, causes a delay in bone growth, but the exact mechanisms of the delay are still debated [27]. The effects of diabetes on bone healing have generally been studied between a few weeks to a few months into the healing process [79], [80] and less research has studied the effects of diabetes on bone growth in the early stages of bone healing [69]. The early stages of bone healing have generally been accepted to largely determine the long-term success of endosseous implants [69]. Therefore, it has been suggested that this critical delay in bone formation seen in hyperglycemic groups is strongly influenced by the early stages of bone growth. It has been shown as early as five days into the bone healing that bone volume is much less in diabetic bone than control groups [69].

Currently, there are gaps in the knowledge regarding the nanostructure of diabetic bone that need to be investigated, particularly in the critical early stages of bone formation. Preliminary research on diabetic bone healing has proposed that compromised intrafibrillar mineralization in hyperglycemic groups could be a reason for this delay and ultimately result in the increased implant failure rates seen in hyperglycemic groups in literature [27]. The hypothesis in this thesis research project is that diabetic animal models have reduced bone quality in the critical stages of early bone formation indicated by an increased porosity, decreased mineralization level, and compromised intrafibrillar mineralization pattern.

The purpose of this research project was to identify structural and compositional differences in hyperglycemic bone formation compared to normal bone formation at a five-day time point of bone growth, using high-resolution microscopy techniques which can be used to analyze the ultrastructure of bone. In particular, the research investigated differences in hyperglycemic compared to control groups in bone porosity, relative mineralization, collagen morphology, collagen-mineral structural arrangement, and elemental analysis of calcium and phosphorous components of bone.

1.4 SURGICAL MODEL SELECTED

1.4.1 STREPTOZOTOCIN DRUG INDUCED RAT MODEL

The inconsistency seen in diabetic research, particularly T2DM, has been suggested to be due to differences in the type of bone, the anatomical region of bone, and the animal model used in each study, which makes it difficult to compare studies across literature [49]. The animal model chosen for this research project was streptozotocin (STZ) induced male Wistar rats, which is a common animal model used for studying diabetes [81]. Alloxan is another drug that can be administrated to induce diabetes; however, it is important to note that the dosage range to induce

diabetes with this drug is narrow and even a light overdose can cause general toxicity to the animal model [81]. It has been shown that experimental diabetes can be induced between two to four days using intravenous injections of 60mg/kg STZ in adult Wistar rats [82]. Using this method it has been reported that the average glucose levels for the normal and hyperglycemic rats are 7.5mmol/L and 27.7mmol/L respectively, similar to normal and diabetic glucose levels seen in humans [82], [83]. According to the World Health Organization, normal glucose tolerance in humans does not usually exceed plasma glucose levels of 7.8mmol/L whereas diabetic individuals plasma glucose levels are higher than 7.8mmol/L [83].

While induced hyperglycemia with STZ can be experimentally reproducible, STZ induced animal models are more similar to T1DM rather than the more common T2DM seen in humans [81], [82]. When STZ enters the body, it induces a cellular toxic response to the Islets of Langerhans beta cells in the pancreas [82]. The drug enters the pancreatic beta cells through channels in the plasma membrane. It has been shown in mouse models that a high dosage delivery, rather than a multiple-low dose delivery, may cause a more severe form of diabetes. Variations in dosage amounts and delivery times may also contribute to the differences seen in literature regarding experimental diabetes [84].

1.4.2 OSTEOTOMY SURGERY

Two different models used to study bone healing include osteotomy and fracture models. The osteotomy model is a surgically invasive procedure that involves drilling a hole with a precise diameter into the bone. The fracture model involves fracturing the bone. However in the fracture model, it is difficult to know what type of fracture will be produced. Therefore, the osteotomy model has some advantage over the fracture model including: being site specific, defect size specific, and experimentally reproducible [85].

The diaphysis of the femur is a preferred anatomical region to choose to study bone growth as it is mainly composed of cortical bone, which is much less porous than trabecular bone or new bone, making it easier to visualize differences between cortical and newly formed bone [11].

1.5 MICROSCOPY AND PREPARATION TECHNIQUES

1.5.1 MICRO-COMPUTED TOMOGRAPHY

Micro-computed tomography (micro-CT) is a non-destructive 3 dimensional (3D) imaging technique which uses an X-ray source. The X-rays are projected through the sample onto the X-ray detector on the other side of the sample. During the scan, the sample is rotated 360 degrees while 2 dimension (2D) X-ray projection images are acquired from varying angles, which can mathematically be interpreted into an image with 3D information [86].

The internal structure of an object can be imaged using X-rays. As the X-rays pass through the sample, some X-rays will not pass through object and therefore not reach the detector while others will pass through the object to the detector. A principal criteria which will determine if X-rays can pass through the absorbing material is its atomic number (Z). X-rays will interact more with absorbing materials with a higher Z than materials with a lower Z, providing contrast difference in the projection images (i.e. raw data) largely based on Z but also dependent on the density of the object. Therefore, the more the X-rays interact with the material the less X-rays will be detected by the detector and the darker the region will appear, causing heavier elements to be darker and lighter elements to be lighter in the projection images [86].

The projection images can then be used to create 2D reconstructions, where the user selects image contrast limits to make a binary image. These 2D reconstructions can then be used to make

a 3D model using various reconstruction software algorithms [86]. This makes micro-CT a very good technique for analyzing bone, especially measuring cortical and trabecular morphology [87].

1.5.2 SCANNING ELECTRON MICROSCOPY

Scanning electron microscopy (SEM) is an electron microscopy technique where a primary electron beam, emitted from an electron gun, is accelerated and focused through various electromagnetic lenses to a fine point on the sample, which is mounted on an electron conducting SEM stub. The electron beam is then scanned in a raster pattern across the sample by scanning coils [88]. The SEM is under vacuum, as air would interfere with the electron beam path. The higher the energy (keV) of the incident electron beam, the greater the penetration depth into the sample [6].

The rastered incoming electron beam produces many signals including secondary electrons (SE) and backscattered electrons (BSE). SE are relative lower energy electrons, which escape from near the top of the sample and provide mainly topographical information. BSE are elastically scattered electrons which have interacted with the atomic nuclei of the sample. These electrons are produced from deeper within the sample and provide mainly compositional information based on the atomic mass of the sample, where elements with higher atomic numbers appear brighter [6] (Figure 1.5). Therefore, in bone samples, the more mineralized regions appear brighter in BSE mode [89]. For non-conductive samples, such as bone, it is important to coat the top and paint side of the sample with conductive elements, such as gold and nickel respectively, to reduce charging and ensure that electrons can be grounded [88], [89].

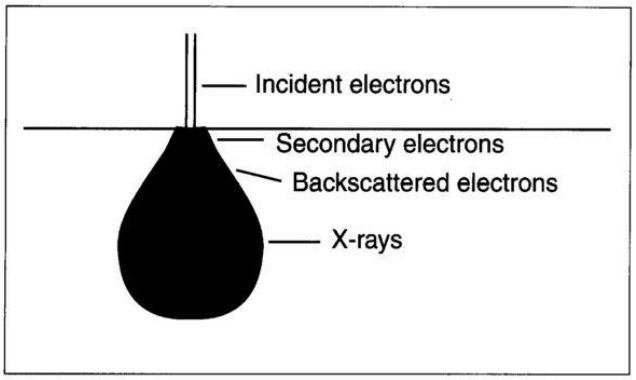

Figure 1.5 SEM Signals Produced by Incident Electron Beam. The incident electron beam is accelerated and focused to a fine point on the sample where it interacts with the sample to produce multiple signals including secondary electrons (SE) from the top of the sample and backscattered electrons (BSE) from deeper within the sample. Adapted and with permission of use from [6].

1.5.3 RAMAN SPECTROSCOPY

Raman spectroscopy is a type of vibrational spectroscopy, which can be used to characterize the chemical composition of a sample. The Raman spectrometer is typically equipped with an optical microscopy which allows for micro-spatial mapping of the chemical composition [14]. Raman spectroscopy works by emitting a laser onto the sample. When the laser hits the sample most of the light reflected from the sample will have the same wavelength as the emitting laser wavelength. However, a small fraction of photons will be scattered at a wavelength different from the wavelength of the incident light due to the molecular vibrations in sample. The characteristic wavelength differences can be used determine a distinct spectra for the sample [90].

The ability of Raman spectroscopy to micro-spatial map the chemical composition of a sample can be useful for determining bone quality [14]. In particular, it can be used to calculate the relative mineralization of bone by measuring the mineral to matrix ratio using any of the following peaks: PO_4^{-3} $v1$/Amide I, PO_4^{-3} $v1/CH_2$ wag, and PO_4^{-3} $v1$/Amide III (Figure 1.6). The

wavenumber used to calculate the area under these peaks are as generally as the following: PO_4^{-3} *v*1 between 1055-1090cm^{-1}, CO_3^{-2} *v*1 between 1220-1300cm^{-1}, Amide III between 1410-1490cm^{-1}, CH_2 wag between 1410-1490cm^{-1}, and Amide I between 1550-1720cm^{-1} [7]. Samples can also be mounted onto gold slides to reduce signals from the background during Raman analysis, resulting in more accurate chemical characterization [91].

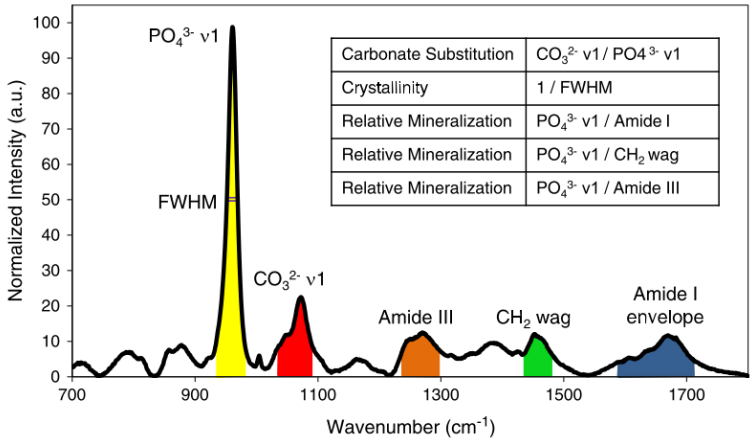

Figure 1.6 Typical Raman Spectrum of Bone. The relative mineralization of bone can be calculated under the area under the different peaks highlights with arbitrary colours and stated in the chart on the Figure, with permission of use from [7].

1.5.4 TRANSMISSION ELECTRON MICROSCOPY

Transmission electron microscopy (TEM) is a high-resolution electron microscopy technique where an accelerated beam of electrons, from an electron emission source, passes through electromagnetic lenses and apertures to be transmitted through an electron transparent specimen, which is usually less than 100nm thick. The microscope is operated under vacuum to prevent air from interfering with the electron beam path. As the beam passes through the specimen, it interacts with the specimen to produce multiple signals that can be used to create images with contrast differences [92].

Different contrast modes provide distinctive information about the sample. TEM can be operated in diffraction mode or imaging mode. Diffraction mode can be used to acquire selected area electron diffraction (SAED), which provides information about the crystalline structure [92]. In particular, it can help determine the texture of the crystals. Figure 1.7 shows a typical SAED for mature bone which illustrates intrafibrillar mineralization patterns where the (002) plane appears as arcs, oriented along the long axis of the collagen fibril, marked by the double headed white arrow. This indicates that the c-axis of the bone mineral is aligned with collagen fibrils in mature bone. During the early stages of the mineralization process the SAED wouldno preferred texture or orientation of the bone mineral, since it is not organized along the length of collagen yet. This would be represented by a lack of defined (002) arcs, and amorphous mineral would be identified by a diffuse band around the central bright SAED spot. Nano-crystalline structures may have similar SAED patterns to amorphous structures as the wide variety of crystal orientations would cause diffraction in all planes, creating a diffuse like band as well, lacking preferred texture [8].

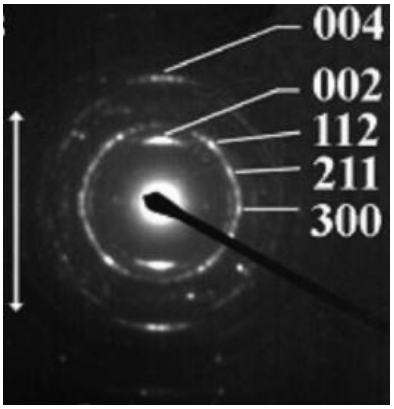

Figure 1.7 Selected Area Diffraction Pattern of Bone. A selected area electron diffraction (SAED) illustrating intrafibrillar mineralization of equine cortical bone. The arcs (002) and (004) are parallel to the long axis of the collagen fibril. The direction of the collagen fibril is shown by the white arrow. Adapted and with permission of use from [8]**.**

In imaging mode, a TEM image can be acquired in either bright-field (BF) or dark-field (DF) imaging. The contrasts formed in both imaging methods are dependent on the thickness and mass of the specimen. BF uses the unscattered electrons to construct an image, where heavy elements appear darker. DF on the other hand uses scattered electrons to construct an image, where the electrons scattered along a selected direction appear brighter [92] (Figure 1.8).

In scanning transmission electron microscopy (STEM), as compared to conventional TEM, the electron beam is focused in a convergent beam and scanned across the sample, whereas in normal TEM a parallel beam is used and this scanning process does not occur [92]. In STEM, high angle annular dark field (HAADF) can be operated to acquire scattered electrons from a larger angle than conventional DF [92].

Two types of chemical analysis in the TEM are energy dispersive X-ray spectroscopy (EDS) and electron energy loss spectrometry (EELS). EDS, which is better for identifying heavier elements detects X-rays generated by the electron beam and separates them according to their energy into a spectrum which can then be used to quantify elements [92]. EELS on the other hand provides better spatial resolution and is better at detecting light elements than EDS. When the incident electron beam interacts with the inner-shell electrons of specific atomic elements of the sample, inelastic scattering of electrons will occur, resulting in a characteristic amount of energy loss of the incident beam, which can be measured by EELS [9], [93].

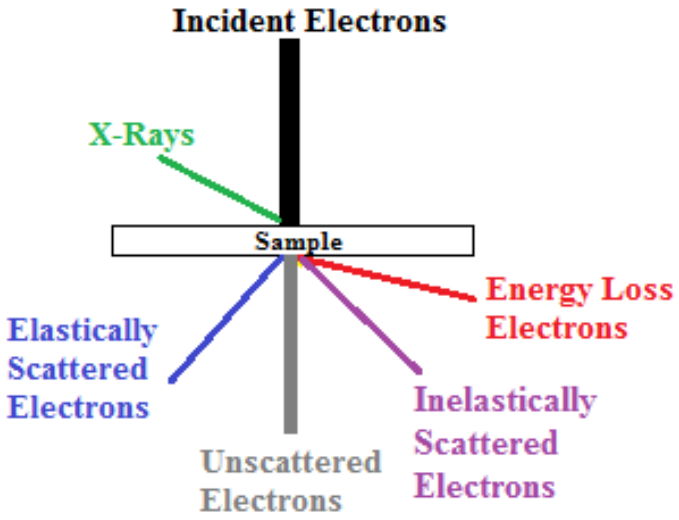

Figure 1.8 Interaction of Incident Electron Beam with a Thin Sample. When an electron beam is accelerated and focused on a thin sample it produces multiple signals of which some can be seen in this Figure. A BF image using unscattered electrons whereas a DF image uses scattered electrons. The analytic techniques EDS and EELS detect X-ray and energy loss electrons, respectively. Based on Figure from [9].

Preparation for TEM is commonly done using a focused ion beam (FIB) or an ultramicrotome. FIB is a site specific preparation method where SEM images are taken during a milling process, performed by a gallium ion beam being accelerated towards the sample. This ion gun, along with an electron beam, can be controlled such that a nano-sized, electron transparent lift out can be removed from the region of interest (ROI) for further analysis. The other technique, ultramicrotoming, can use a diamond blade to make uniform electron-transparent sections of bone. In both methods, the TEM sample is placed on a TEM grid. FIB prepared samples are attached to TEM grids via an *in situ* TEM lift-out method. The ultramicrotome prepared samples are floated on water and usually placed on copper, nickel, or gold based grids, with varying mesh sizes and shapes depending on the sample type. The TEM grid typically has a carbon or polymeric support film which is amorphous, thin, and has a low electron density [94]. Staining is useful to enhance contrast of the sample. In electron microscopy, the most common staining used for ultrathin

sections of bone is a double contrast method. This double contrast method, which is also used for other samples besides bone, uses uranyl acetate and lead citrate to interact with lipids, proteins, and glycogen in the sample [95].

CHAPTER 2

MATERIALS AND METHODS

2.1 SAMPLE PREPARTION

2.1.1 STREPTOZOTOCIN INDUCTION AND SURGERY

A total of ten Wistar rats between four and five months old weighing between 200-250g were used in this study as an animal model. All animal experiments, which were carried out by our collaborators, Dr. John Davies and his research group, were approved by the Ethics Committee of Animal Research at the University of Toronto and received animal tissue ethics board clearance at McMaster University. Five rats in the normal, i.e. control, group were injected intravenously with 0.9% sterile saline and another five rats were injected with 65mg/kg of STZ to induce diabetes, i.e. the hyperglycemic group (Figure 2.1). A representative sample (one rat from each metabolic group) of glucose levels were recorded pre-injection and post-injection prior to surgery for both metabolic groups (Table 2.1).

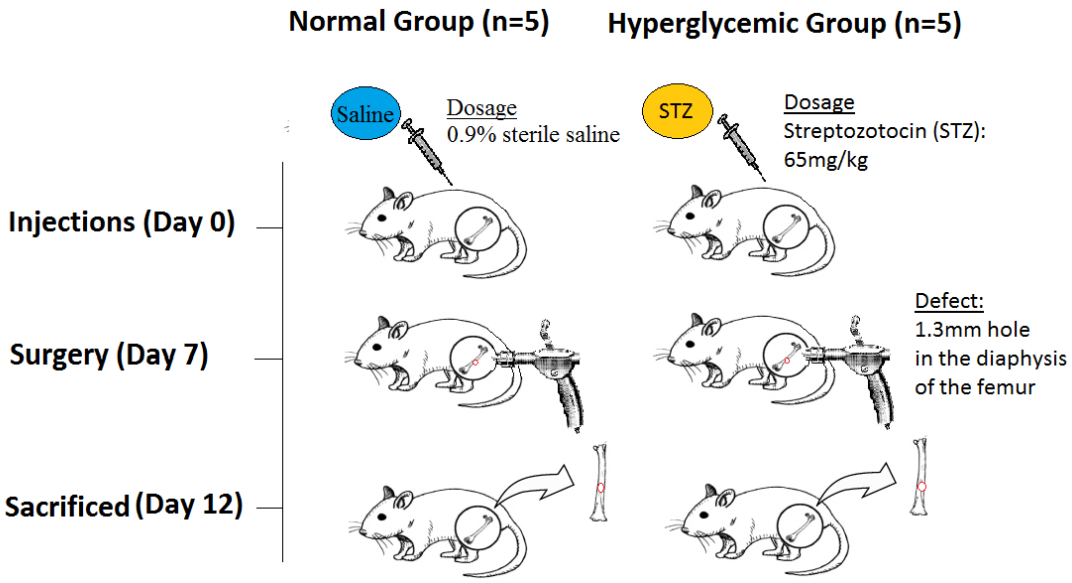

Figure 2.1 Hyperglycemic Induction. Five rats from the normal group were injected intravenously with 0.9% saline and five rats from the hyperglycemic group were injected intravenously with 65mg/kg of streptozotocin (STZ).

Table 2.1 Glucose Levels. A representative sample (one rat from each metabolic group) of the recorded glucose levels used to determine if the rats became hyperglycemic after STZ-injection compared to control group.

Time	Normal (mmol/L)	Hyperglycemic (mmol/L)
Pre-Injection	7.4	5.4
24hrs Post-Injection	5.3	14.1
48 hrs Post-Injection	5.7	18.2
72 hrs Post-Injection	5.2	13.2
Surgery (5 days Post-Injection)	5.7	15.7

The rats were deemed hyperglycemic if and when their blood glucose level was greater than 15mmol/L in the first 48 hours after injection. Rats were induced with 4% Isoflurane 1.5L O_2 per minute and a 1.3mm defect in the diaphysis of the (right or left) femur (depending on specific rat) was made using an osteotomy model. Throughout surgery rats were administered 2.5%

Isoflurane. This initial drilling surgery was conducted 7 days after the injections were administered. The rats were then sacrificed five days post-surgical drilling, via exposure to CO_2 followed by cervical dislocation, and their femurs were harvested. Once the femurs were harvested from the rats, cross-sectional cuts were made in the diaphysis to isolate the region of interest (ROI). For more information on how Dr. Davies and his research group at U of T conducted their surgical procedure, euthanasia, and sample harvesting refer to the paper by Ajami, et al. [27].

2.1.2 FIXING AND EMBEDDING PROCESS

Our collaborators at U of T were also responsible for fixing and embedding the femurs. The bone was fixed in Karnovsky's Glutaraldehyde solution. The samples were then dehydrated in ethanol using the following series: 70% ethanol for 10 minutes, followed by 100% ethanol for 25 minutes, and lastly with 100% propylene oxide for 30 minutes. The samples were then embedded in EMbed812 and the molds were cast in an oven at 60º Celsius for 24 hours. The samples were then delivered to McMaster University from U of T for microscopical analysis (Figure 2.2).

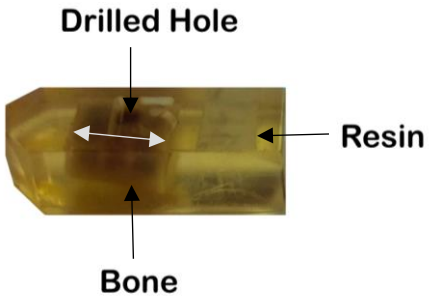

Figure 2.2 Embedded Rat Femur. One of the delivered samples from the University of Toronto, representative of all samples. In this sample the long axis of the femur is illustrated by the double pointed white arrow.

2.2 EXPERIMENTAL PROCEDURE

2.2.1 MICRO-COMPUTED TOMOGRAPHY

A SkyScan 1172 Scanner (Bruker MicroCT, Kontich, Belgium), a high resolution micro-CT system, was used to acquire X-ray scans of the normal and hyperglycemic samples with a camera pixel size of 8.68µm, image pixel sizes between 1.7 and 6.8 µm, with a source voltage between 85 and 86 keV, a source current of 116 µA, and a rotation step between 0.3 and 1.0 degrees. Reconstructions from the scans were created using NRecon software (Bruker MicroCT). The software CTAn (Bruker MicroCT) was used to reduce the file size of the data, via cropping the image, to be uploaded into the visualization software Avizo 9 (FEI Company, Eindhoven, Netherlands). Avizo 9 was then used to segment, based on intensity and location, the newly formed bone from the old bone (i.e. cortical bone) and the resin. Figure 2.3B shows the segmented version of Figure 2.3A with the arbitrary colours green, blue, and purple clearly representing the old bone, new bone, and bone marrow, respectively. Avizo 9 was also used to visualize a 3D model from the reconstructions.

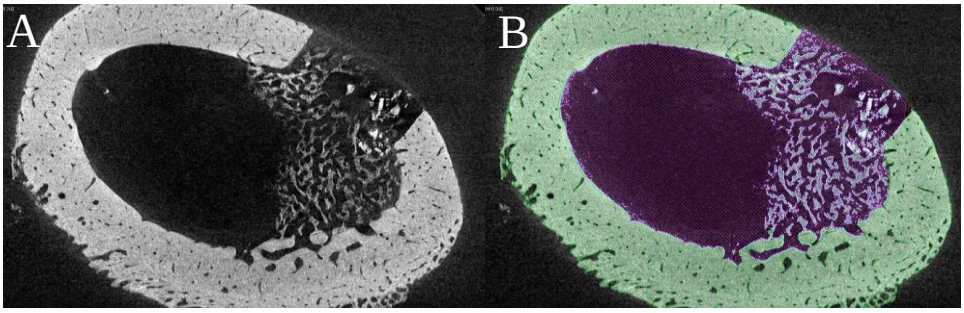

Figure 2.3 Image Segmentation of Micro-CT X-ray Scans. A) A 2-D slice throughout the reconstruction illustrating a cross-sectional view about one third of the way into the osteotomy site where bone growth occurred. The white regions show the bone and the black regions are where the resin is located. B) A segmented version of the 2D reconstruction. The labels, with arbitrary colours, represent the following: green is the cortical bone, blue is the new bone, and purple is the bone marrow.

This reconstruction was then used to calculate the volume of the old bone, newly formed bone, and resin. Then the relative porosity was calculated for different sub-volume ROIs of the newly formed bone using the formula:

$$\text{Porosity} = \frac{\text{volume of resin}}{(\text{volume of resin} + \text{volume of new bone})} \times 100\%$$

To calculate the new bone porosity using the micro-CT images a total of 12 sub-volume ROI for the normal group (from two of the normal samples) and 11 sub-volume ROI for the hyperglycemic group (from two of the hyperglycemic samples) were selected. The average porosity of the new bone from the normal and hyperglycemic groups were statistically compared using a two-tailed t-test in Microsoft Excel. A two-tailed t-test in Microsoft Excel was also used to compare samples within their respective metabolic group.

The porosity was calculated using a volume to volume based method. Figure 2.4 shows the process of how the sub-volumes, with the dimension of 0.5mm x 0.5mm x 0.5mm, were extracted from the 3D segmented models. The locations were selected from regions where new bone was present throughout the entire ROIs. This was done to keep a consistent comparison between the normal and hyperglycemic sample. Figure 2.4A shows an example ROI of the location where the sub-volume was extracted and Figure 2.4B illustrates the porous newly formed bone structure (i.e. the grey structure). Figure 2.4C is an arbitrary coloured segmented version of Figure 2.4B, with the green representing the newly formed bone and the red representing the bone marrow.

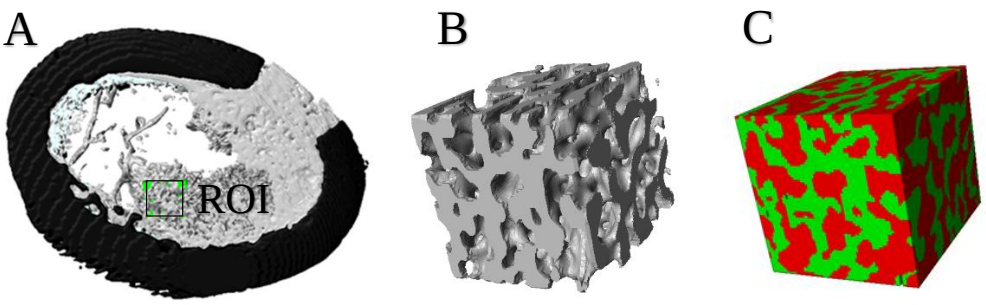

Figure 2.4 ROIs Selection of Newly Formed Bone Sub-Volumes from Micro-CT 3D Models. The method used to measure the porosity from the micro-CT images reconstructions. A) A representative of where the ROIs of newly formed bone with the dimension of approximately 0.5mm x 0.5mm x 0.5mm were chosen from the micro-CT 3D model. B) The ROI sub-volume corresponding to the ROI in image to the left used to calculate the porosity. C) The segmented ROI with the green representing the newly formed bone and the red representing the bone marrow.

2.2.2 SCANNING ELECTRON MICROSCOPY

A Buehler IsoMet Low Speed Saw, with a diamond blade, was used to remove excess resin surrounding the bone. Sandpaper with a 600 grit size was used to expose the site of new bone formation in the surgical cavity and the exposed bone was finely polished with P4000 silicon carbide for electron microscopy imaging. The samples were mounted onto a SEM stub and nickel paint was coated along the side of the sample. The exposed bone was coated with gold for one minute, using an Edwards S150B Sputter Coater, resulting in approximately a 10-20 nm thick layer of gold on the exposed region of the sample. A JSM-6610LV (JEOL, Montreal, Canada), a tungsten filament equipped SEM, was used to image the exposed surface of the samples. The SEM was operated with voltages ranging from 10-15 keV depending on the sample and micrographs were obtained in BSE mode.

ImageJ software (Fiji, National Institutes of Health, Bethesda, U.S) was used to calculate the closed porosity of the new bone from the 2D SEM images of both metabolic groups. Our

research defined closed porosity as the pores that were fully enclosed by surrounding bone in the 2D micrographs. The porosity of different ROIs of the newly formed bone were calculated using the formula:

$$\text{Porosity} = \frac{\text{area of resin}}{(\text{area of resin} + \text{area of new bone})} \times 100\%$$

To calculate the new bone porosity using the SEM images a total of 37 bone segments from the normal group and 25 from the hyperglycemic group were randomly selected among regions from all ten samples (i.e. five hyperglycemic and five normal). Statistical analysis was completed using a two-tailed t-test in Excel 2013 to compare the calculated closed porosity of the newly formed bone from the normal and hyperglycemic samples.

Figure 2.5 shows the image processing steps which allowed the new bone to be differentiated from the resin in order to calculate the closed porosity. Figure 2.5A shows the acquired SEM images in BSE mode, where brighter regions are bone. As it is difficult to consistently differentiate osteocyte lacunae from other pores in the SEM acquired images, the closed porosity was defined in this research to include all porous areas, including osteocyte lacunae. Figure 2.5B and C are intermediate image processing steps: in Figure 2.5B a threshold was applied, and Figure 2.5C illustrates another intermediate step to eliminate background noise due the resin. The different segment regions in Figure 2.5C are represented by arbitrary colours.

Figure 2.5D was the final image in the image processing, which was used to calculate the porosity, with the grey regions representing the new bone and the white regions representing the pores.

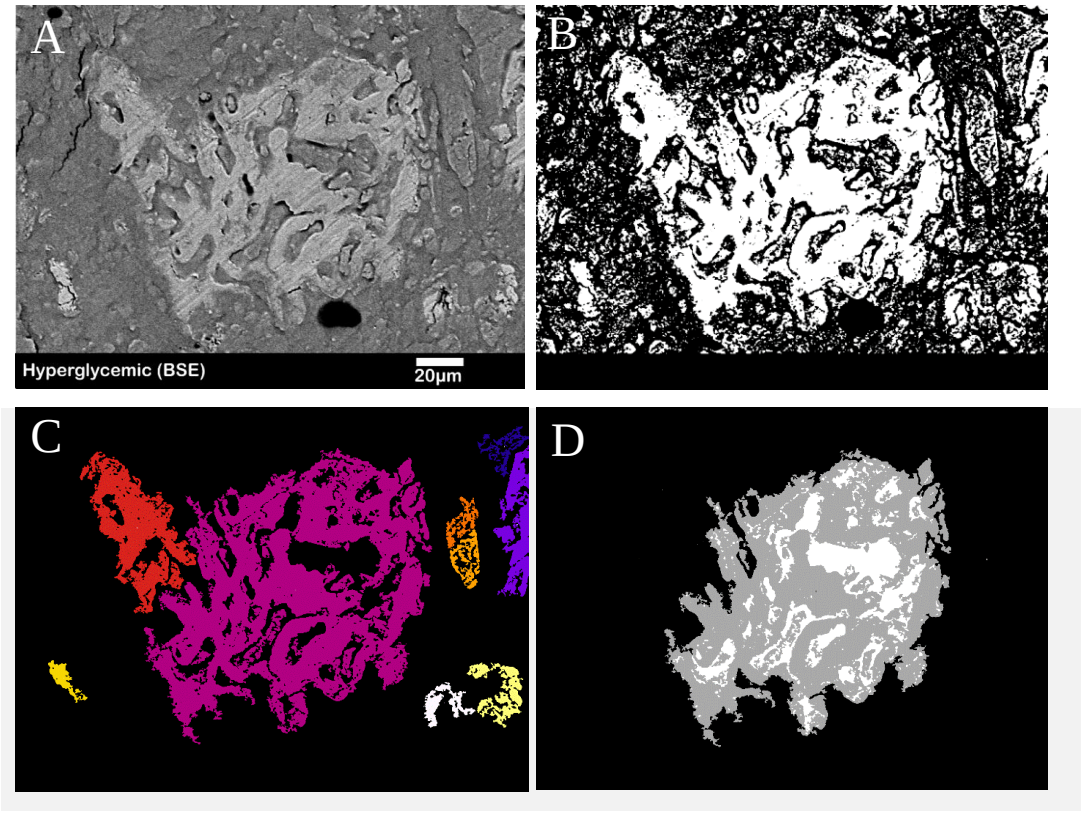

Figure 2.5 Image Segmentation of SEM Images. An example of the imaging process used to calculate the 2D porosity. A) An original micrograph acquired using SEM in BSE mode. B) The image after a median filter and a threshold was applied to the image to separate the newly formed bone from the resin. The small white particles surrounding the newly formed bone are noise. C) Another intermediate image processing step that excluded small particle sizes to reduce noise and categorize different segments into different regions. The red and pink illustrate bone segments, the black is the background, and the other colours are noise. D) The final segmentation corresponding to the newly formed bone were selected and the pores, in grey and white respectively used to calculate 2D porosity.

2.2.3 RAMAN SPECTROSCOPY

Sections with a thickness of 1 µm from regions with new bone formation for both the normal and hyperglycemic samples were prepared using a Leica UCT Ultramicrotome equipped

with a diamond blade. These bone sections were then mounted onto gold coated glass slides for Raman spectroscopy. An inVia dispersive Raman microscope (Renishaw, Wotton-under-Edge, UK) equipped with a 785 nm excitation source was used to examine the samples. Using the WiRE 3.4 software package (Renishaw), the excitation source coupled with the 1200 lines/mm diffraction grating was used to collect the Raman data. Line spectra were collected between 700 cm^{-1} and 1750 cm^{-1}, with an exposure time of 10 seconds on the CCD detector. A step size of 2µm was used at a magnification of 50 times. Individual spectra were extracted from the line map image and processed in OMNIC 8.0 software (Thermo Fish Scientific, Waltham, United States). Automatic baseline corrections were performed and the areas under the phosphate peak, between 930-980 Raman shift (cm^{-1}), and the methylene peak, between 1550-1720 Raman shift (cm^{-1}), were used to measure the relative amount of mineralization (i.e. PO_4^{-3} $\nu 1$ to CH_2 wag ratio) in the ROIs.

2.2.4 FOCUSED ION BEAM FOR TEM PREPARATION

A Zeiss NVision 40 (Carl Zeiss, Oberkochen, Germany), a FIB milling instrument with a Schottky Field Emission Gun (FEG) filament SEM, was used to prepare site-specific sections for TEM (Figure 2.6A). ROIs between an osteocyte and the mineralized front of the newly formed hyperglycemic and normal bone were chosen (Figure 2.6B). Figure 2.6C shows a protective layer of tungsten deposited onto the ROI. A gallium ion beam was used to mill around the ROI (Figure 2.6D). Then an *in-situ* micro-manipulator was used to move the ROI sample and place it onto a TEM grid (Figure 2.6E). The ROI was thinned with the ion beam until it was electron transparent (Figure 2.6F). Then an Edwards S150 Carbon Evaporation Source was used to carbon coat the TEM grids for 15 seconds, resulting in a thickness of approximately 3-10nm, to reduce charging during TEM imaging.

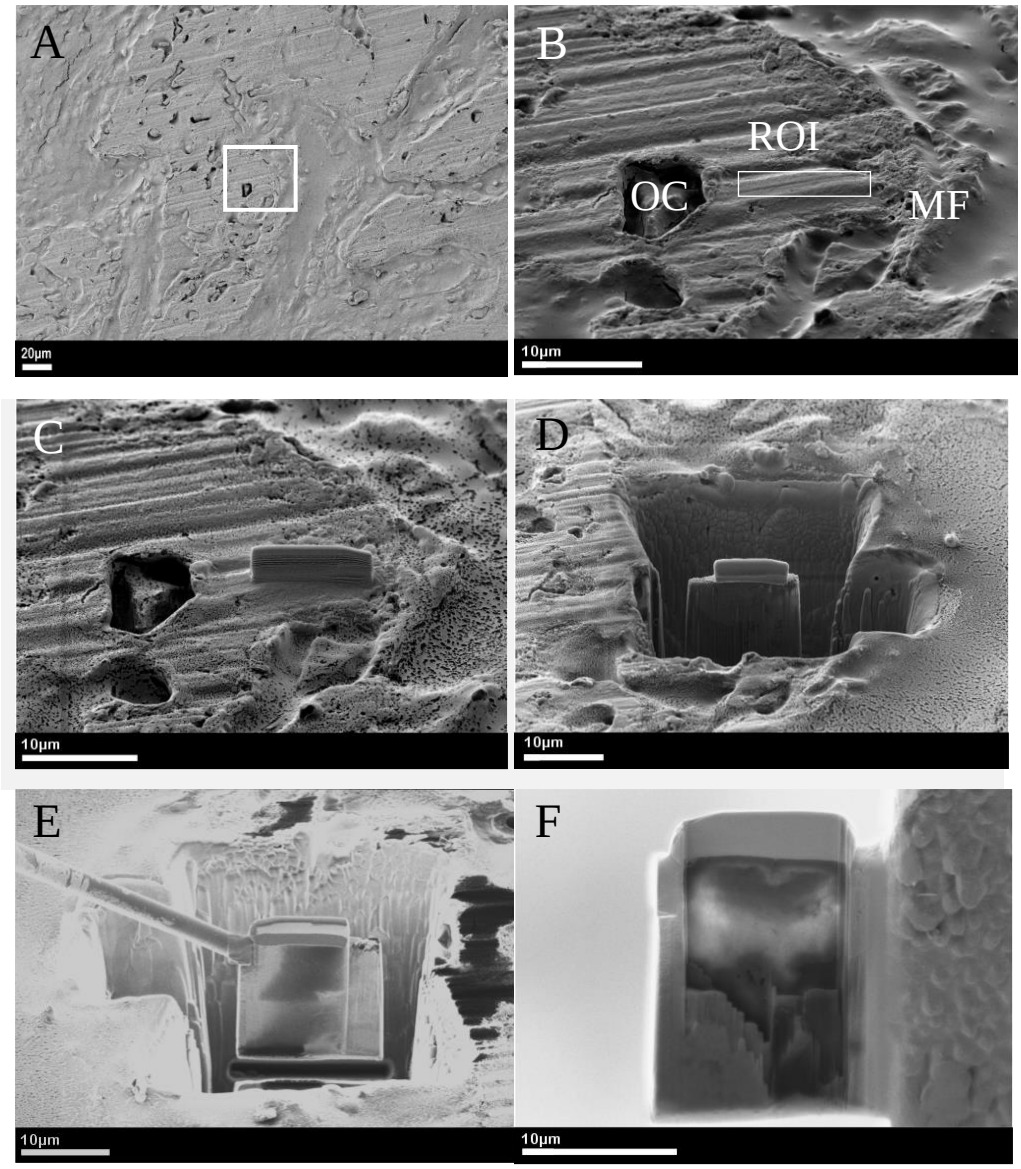

Figure 2.6 Focused Ion Beam (FIB) Lift-Out Method. All of the micrographs were collected in secondary electron (SE) mode in SEM. A) Overview of the newly formed bone. The white box is magnified in the image to the right. B) Higher magnification of the corresponding image to the left, where the ROI between an osteocyte (OC) and the mineralized front (MF) is shown. C) Tungsten deposition over the ROI. D) Image after the gallium ion beam milled around the ROI. E) Microneedle attachment to the ROI. F) The electron transparent sample thinned by an ion beam and then attached to a TEM grid.

2.2.5 ULTRAMICROTOME FOR TEM PREPARATION

A Leica UCT Ultramicrotome, equipped with a diamond blade, was used to make approximately 100 nm thick sections of the ROIs from with the newly forming bone from the osteotomy site for the normal and hyperglycemic samples. The sections were placed onto formvar-coated copper grids. The sections were post-stained with uranyl acetate and lead citrate. The TEM grids were then carbon-coated with an Edwards S150 Carbon Evaporation Source for 15 seconds resulting in an approximately 3-10nm deposition of carbon on the sample, to minimize charging during TEM imaging

2.2.6 TRANSMISSION ELECTRON MICROSCOPY

The FIB prepared samples were viewed with a Titan 80-300LB (FEI Company, Eindhoven, Netherlands) microscope, operated in STEM mode at an acceleration voltage of 300 keV, where the HAADF detectors were used to image these samples. The ultramicrotome prepared samples were imaged in JEM 1200EX TEMSCAN (JEOL, Peabody, USA) operated at an accelerating voltage of 80 keV. The images were acquired with an AMT 4 megapixel digital camera (Advanced Microscopy Techniques, Woburn, USA). The average diameter and average D-spacing of collagen fibrils were measured from the micrographs using Image J software. To calculate the average collagen diameter, 280 line measurements were taken along the diameter of the collagen fibrils near the mineralized front for both the normal (from two normal samples) and hyperglycemic (from two hyperglycemic samples) groups. To calculate the average D-spacing, 160 line measurements were taken from various regions of D-spacing along the collagen fibrils. Statistical analysis was computed in Microsoft Excel 2013 using a two-tailed t-test comparing the normal and hyperglycemic measurements.

SAED, EDS, and EELS, along with corresponding HAADF images from the ultramicrotomed samples, were recorded on a JEOL 2010F TEM/STEM (JEOL, Tokyo, Japan) operated at 200 keV. SAED and EDS spectra were collected from three main ROIs including old bone, mineralized islands, and collagen fibrils surrounding these mineralized islands. A two tailed t-test in Microsoft Excel 2013 was used to compare the average Ca/P ratio obtained using EDS spectra between the mineralized islands in normal and hyperglycemic groups. The average Ca/P ratio was calculated from eight different mineralized islands from the normal (two normal samples used) and eight different mineralized islands from the hyperglycemic (two hyperglycemic sample used) groups. EELS maps were obtained from regions along the collagen fibrils protruding from the mineralization islands. The EDS and EELS raw data was processed in Digital Micrograph software (Gatan Microscopy, Pleasanton, United States).

CHAPTER 3

RESULTS AND DISCUSSION

3.1 BONE POROSITY

Research has suggested that bone defect healing in rat animal models is only disrupted in the early bone healing phases [69], [96]. For example, it has been demonstrated using SEM imaging that bone healing is disrupted in diabetic rats 14 and 24 days post-surgical drilling and no differences in bone formation are seen 42 days post-surgery [96]. Micro-CT is another technique that has been used to study diabetic bone healing. It has shown, that diabetic bone has a lower defect healing rate 12 weeks post-surgical drilling [60]. However, research done by our collaborators has shown delayed bone healing in hyperglycemic rat models as early as only five days post-surgical drilling, using micro-CT imaging. This study also found that differences between hyperglycemic samples and controls disappeared 15 days post-surgery [69].

One of the aims of this research was to qualify and quantify differences in the bone microarchitecture at the early time point of bone healing (five days post-surgery) using both SEM and micro-CT imaging as complementary techniques. We aimed to quantify bone porosity, as it is an important factor in bone quality where increased porosity in cortical bone is generally correlated with decreased bone quality [58]. Studies have shown in diabetic bone both an increased cortical bone porosity and no significant abnormalities compared to control groups [58]–[62].

As far as the knowledge in this thesis, little has been done to quantify bone porosity in diabetes at the very early time point of bone healing, which has generally been accepted to be critical in the long-term success of endosseous implants [53]. It was hypothesized that the microarchitecture may be altered in hyperglycemic bone during early bone formation. Specifically,

it was hypothesized that the hyperglycemic group would be more porous than the normal group, contributing to the decreased bone quality and increased implant failure seen in individuals with hyperglycemia.

3.1.1 POROSITY: 3D MICRON-SCALE

Micro-CT was used to compare the 3D porosity between hyperglycemic and normal bone formation. Figure 3.1 shows the segmented 3D models with the black and grey colours illustrating the cortical bone and newly formed bone respectively, for both the normal and hyperglycemic groups. The 3D models qualitatively illustrate less new bone formation in the hyperglycemic sample compared to the normal sample. They also qualitatively show differences in micro-architecture between the normal and hyperglycemic, where the hyperglycemic sample appears to be more porous than the normal sample. The porosity was further quantified using sub-volume calculations (Figure 2.4, refer to materials and methods section). Also notable in the 3D models, the cortical bone geometry in the hyperglycemic sample slightly differs from the normal sample. Since the rats were only induced with STZ for 12 days before they were sacrificed, it was not expected that there would be significant changes in the already formed cortical bone at this time point. Therefore, it was assumed differences in geometry were due to exact location of harvest. This is because the cortical bone geometry varies in thickness and shape along different regions of the diaphysis of the femur [97].

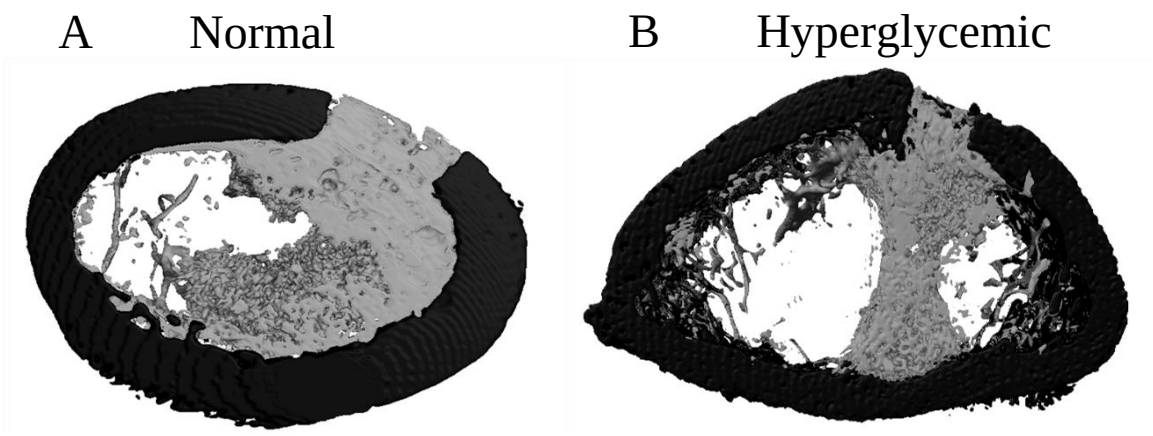

Figure 3.1 Micro-CT 3D Segmented Models. A, B) Segmented 3D models from the micro-CT data for the normal and hyperglycemic samples, respectively. The black regions are the cortical bone and the grey regions are the newly formed bone. The newly formed bone visually appears to be more porous and more structurally disorganized than the surrounding cortical bone. Also, more new bone formation can be visually observed in the normal sample (A) as compared to the hyperglycemic sample (B). In addition, these 3D models suggest the hyperglycemic sample is more porous than the normal group.

The average porosity for the 12 ROIs for the normal sample and the 11 ROIs for hyperglycemic sample were 57.27% and 67.09%, respectively (Table 3.1). A statistically significant result showing an increased porosity for the hyperglycemic sample compared to the normal group ($p < 0.05$) was observed. No statistically significant result was found comparing porosity between samples within their respectively metabolic group (for the normal group $p = 0.64$, for the hyperglycemic group $p = 0.82$). Therefore, this suggests that an increased porosity seen in hyperglycemic new bone formation may play an important role in the increased implant failure rates (due presumably to poor bone quality) seen in hyperglycemic individuals.

Table 3.1 3D Calculated Porosity from Micro-CT 3D Models. 3D calculated porosity from 12 ROIs for the normal samples and 11 ROIs for the hyperglycemic samples. There was a statistically significant result between the normal and hyperglycemic samples ($p < 0.05$) illustrating hyperglycemic new bone formation as being more porous than normal bone formation, but not within samples from the same metabolic group ($p > 0.05$).

Measurements	Normal (ROIs=12)	Hyperglycemic (ROIs=11)
Average Porosity (%)	57.27 ± 7.95	67.09 ± 6.84

Notice in Figure 2.3B (refer to materials and methods section) there are small blue particles the segmented version representing the newly formed bone along the boundary of the bone and resin, which do not appear to be newly formed in the corresponding locations in Figure 2.3A (refer to materials and methods section). These blue particles are attributed to noise from the imaging program when trying to quantify the new bone formation. This will contribute to a minor error in the analysis, with a slight over representation of new bone in the 3D porosity calculation. However, since a similar amount of noise is present in both of the metabolic groups, it should not affect the comparison of porosity between the hyperglycemic and normal groups. The appearance of this noise in micro-CT imaging is why is it also important to use high-resolution imaging techniques, such as SEM, as a complementary technique to better distinguish actual bone from the noise.

3.1.2 POROSITY: 2D SUB-MICRON-SCALE

SEM, a higher resolution imaging technique than micro-CT, was used to detect pores that would be too small to be detected using micro-CT imaging. Figure 3.2 shows a cross-sectional view about one third of the way into the osteotomy site containing the newly formed bone. In the SEM images, the new bone and old bone were distinguish based on consistency of the structure (i.e. with the new bone structure being much more disorganized and porous, and less dense than the cortical bone), contrast, and location within the sample (i.e. the newly formed bone being located within the surgical cavity). In Figure 3.2 there was also a notable change in contrast across the mineralized front of newly formed bone in BSE mode which can be related to apparent mineralization, illustrating the mineralization level decreasing from the centre of the bone towards the mineralized front, where the most recent bone formation had occurred. In Figure 3.2, it appears that the newly formed bone in the hyperglycemic sample is more porous than the normal sample; however, further quantification of the 2D porosity, with multiple ROIs from different samples, showed no difference in 2D porosity between the hyperglycemic and normal groups (Table 3.2).

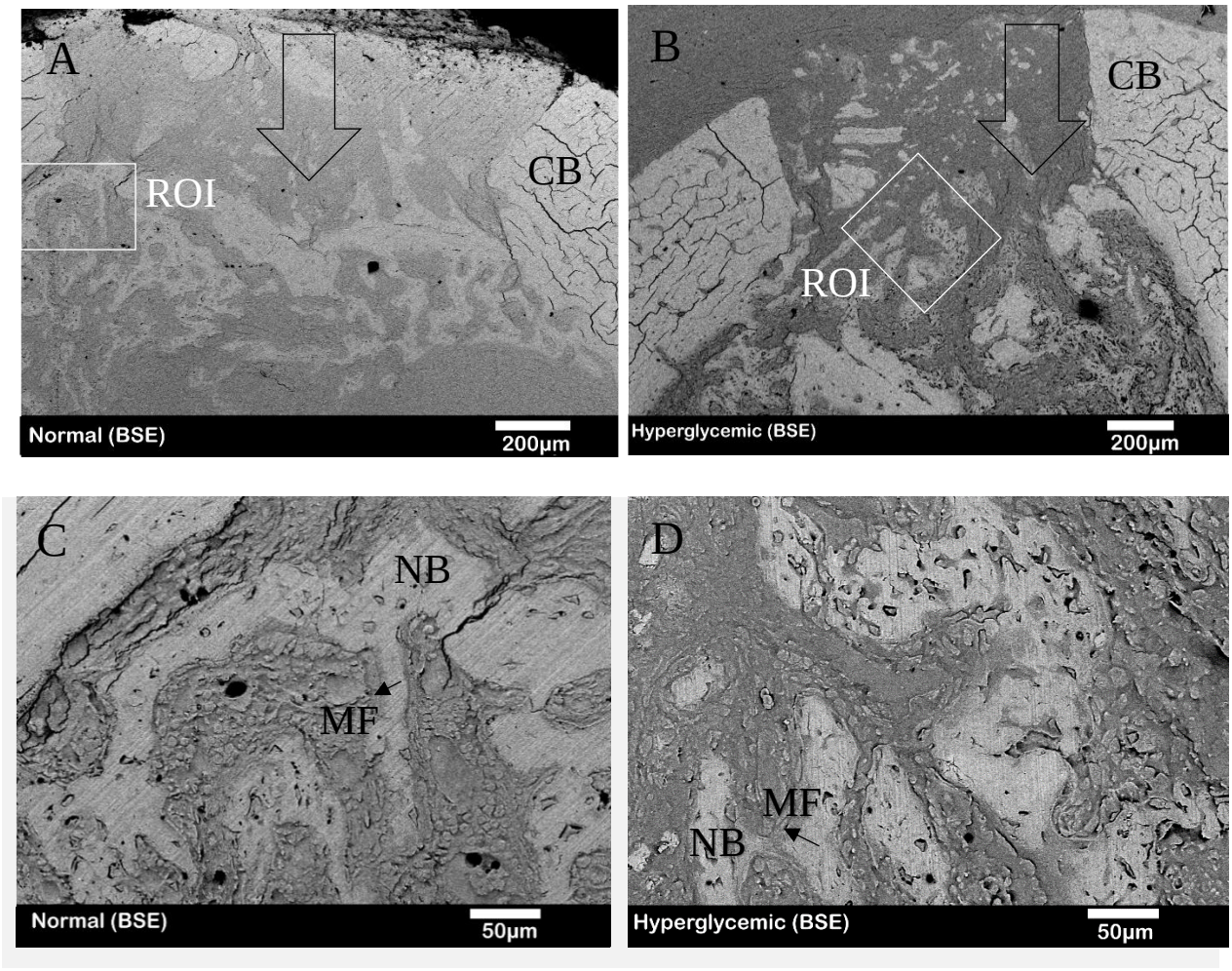

Figure 3.2 BSE SEM images. A) SEM micrograph of the cross-sectional view of the normal bone with the new bone formation inside the surgical cavity. The arrow shows the drilling direction. Seen in the image are both the cortical bone (CB) and where bone growth occurred within the defect area. B) SEM cross-sectional micrograph of the hyperglycemic sample, illustrating similar features as in Figure 3.2A. However, it qualitatively appeared that the hyperglycemic sample was more porous than the normal sample. C, D) Higher magnification of the ROI illustrated in the corresponding images above. The black arrows illustrate the direction towards the mineralization front (MF). A change in contrast is seen along the MF, with the edges of the front appearing less mineralized than the centre of the newly formed bone (NB).

The average porosity of 37 ROIs of the normal newly formed bone was 12.48% and the average porosity for 25 bone ROIs from the hyperglycemic was 14.90%, using 2D SEM imaging

(Table 3.2). These porosity differences were not statistically significant ($p = 0.19$) between the newly formed bone in the normal and hyperglycemic sample groups.

Table 3.2 2D Calculated Porosity from SEM Images. Closed porosity calculations from the 2D SEM micrographs from 37 bone ROIs of the normal samples and 25 bone ROIs of the hyperglycemic samples. After statistical analysis there was no statistically significant differences in the 2D porosity measurements between the hyperglycemic and normal bone ($p > 0.05$).

Measurements	Normal (ROIs=37)	Hyperglycemic (ROIs=25)
Average Porosity (%)	12.48 ± 6.35	14.90 ± 7.95

3.1.3 OVERALL POROSITY

Besides scale, a key difference between the porosity results seen in SEM compared to micro-CT are the imaging limitations used to acquire each set of data. The SEM images were acquired in 2D, meaning that only a slice of the entire structure was imaged, which may not represent the entire 3D bone structure. Micro-CT can be advantageous over SEM as it provides 3D information about the sample. However, the resolution for micro-CT (resolution on the micron-scale) is much less than in SEM (resolution up to the nano-scale). Therefore, as SEM imaging has higher resolution, it is better for detecting the boundaries between the newly formed bone and the pores, meanwhile, the micro-CT has appropriate 3D information at a lower resolution. This makes the comparison of porosity between the micro-CT and SEM good complementary techniques.

The results obtained here suggest that the hyperglycemic newly formed bone is more porous than the normal newly formed bone when the large pores, that might not be included in the high-resolution SEM, are included in the measurements. The observation that the newly formed bone of the hyperglycemic group is more porous than the normal group at the five-day time point

using micro-CT may indicate a decreased bone quality. When bone quality is diminished, the more is more likely to fracture [14]. The difference in the microarchitecture in the hyperglycemic groups compared to controls may contribute to the increased implant failure rate seen in literature [69]. The more porous structure of newly formed bone in the hyperglycemic group compared to controls, can lead to less bone-to-implant contact (BIC), the percentage of bone in contact with the implant. The reduced BIC could inhibit proper osseointegration, especially during the critical early stages of bone healing that have been acknowledged in literature to largely determine the long-term success of endosseous implants [53]. Reduced BIC in diabetic animals has been previously noted in literature [98], [99]. Consequently, the more porous newly formed bone noted in the hyperglycemic group, compared to the normal group, might be less able to support an implant leading to an increase in the implant failure rate in the hyperglycemic group.

3.2 BONE RELATIVE MINERALIZATION

In addition to the microarchitecture of bone, the chemical composition of bone is also a very important factor in bone quality [19]. Relative mineralization level, which can semi-quantify the amount of mineral in an area, can be used to study the chemical composition of bone [7]. An important parameter to consider when studying bone quality is the degree of mineralization of bone (DMB), also referred to as the mineral to matrix ratio which has been suggested to be altered based on remodelling rates [63]. In diabetic groups, DMB has been shown to be both increased and decreased in contradicting research studies [64], [65]. Previous research using Raman spectroscopy has shown an increased mineral to matrix ratio in mature diabetic rat bone (with a PO_4^{-3} $v1$ to CH_2 wag value of approximately 4) compared to control groups (with a PO_4^{-3} $v1$ to CH_2 wag value of approximately 4.5) [7]. They suggest that this difference might be due to AGE-induced crosslinks reducing the vibrational freedom of the collagen leading to a reduced intensity

seen when measuring the matrix signal in diabetic bone [7]. The research in this thesis aimed to semi-quantify how the chemical composition of bone changes across the mineralized front in newly formed bone to provide insight on the bone formation in diabetic groups.

3.2.1 MINERAL TO MATRIX RATIO

Figure 3.3A and B show an overview of typical areas where the ROIs were selected for Raman analysis. Newly formed bone can be seen in the centre of the image, with cortical bone surrounding it. Figure 3.3C and D are magnified regions corresponding to the white boxes in Figure 3.3A and B. Line spectra, taken across the mineralized fronts of the newly formed bone, are shown using black arrows in Figure 3.3C and D, for a normal and hyperglycemic sample respectively. These line spectra were used to determine the relative mineralization across the mineralized front. Figure 3.3E and F illustrate typical Raman spectrums acquired mid-point between the center of the newly formed bone and the mineralized front. The spectra acquired resembled similar bone spectra to those seen in literature [7]. In our research the PO_4^{-3} $\nu 1$ and CH_2 wag peaks were used to calculate the mineral to matrix ratio. Some research also uses the amide I and amide III peaks to measure the matrix [7]; however, the amide I and amide III peaks in these experiments were less pronounced than that of the CH_2 wag. These amide peak may be a result of sample preparation. For example, it has been shown in research that dehydration can reduce the intensity of the amide I peak, since there is a broad water band centered near the amide I peak (around 1 645 cm^{-1}) [100].

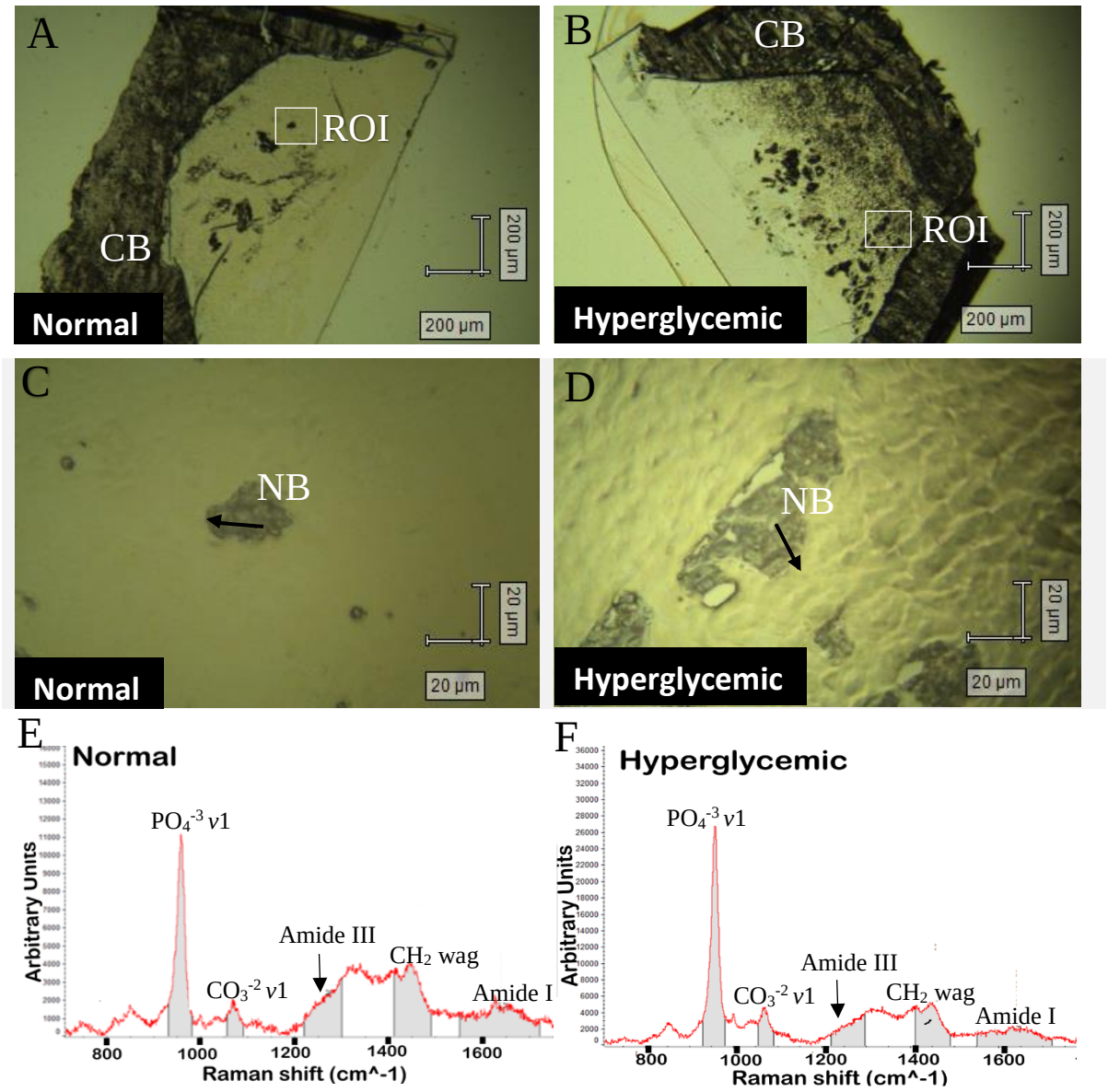

Figure 3.3 Raman Spectroscopy Spectra Maps. A, B) Overview image of the ultramicrotomed sections for a normal and hyperglycemic sample respectively. Seen in the images is the cortical bone (CB) and the newly formed bone inside the hole. C, D) Line spectra were taken across the mineralized fronts of the newly formed bone (NB) for a normal and hyperglycemic sample respectively. The black arrows show the locations where the acquisitions were taken starting from near the center of the newly formed bone towards the mineralized front. E, F) Spectrums taken mid-way between acquisition points to show the different peaks used for relative mineralization calculations for a normal and hyperglycemic sample respectively.

When plotting the mineral to matrix ratio across the line profile, a decrease in relative mineralization along the mineralized front of the newly formed bone is observed in both sample groups (Figure 3.4). Also shown in Figure 3.4, the hyperglycemic sample appears to be more mineralized at the center of the newly formed bone, as the mineral to matrix ratio was larger than the normal sample; however, this was not consistent among all spectra lines (Figures 3.5 and 3.6). Figure 3.4 also shows a more rapid decrease in rate in relative mineralization approaching the mineralization front in the hyperglycemic sample than the normal sample. However, no noticeable consistent trend was observed between the normal and hyperglycemic samples when analyzing the other line spectra (Figures 3.5 and 3.6).

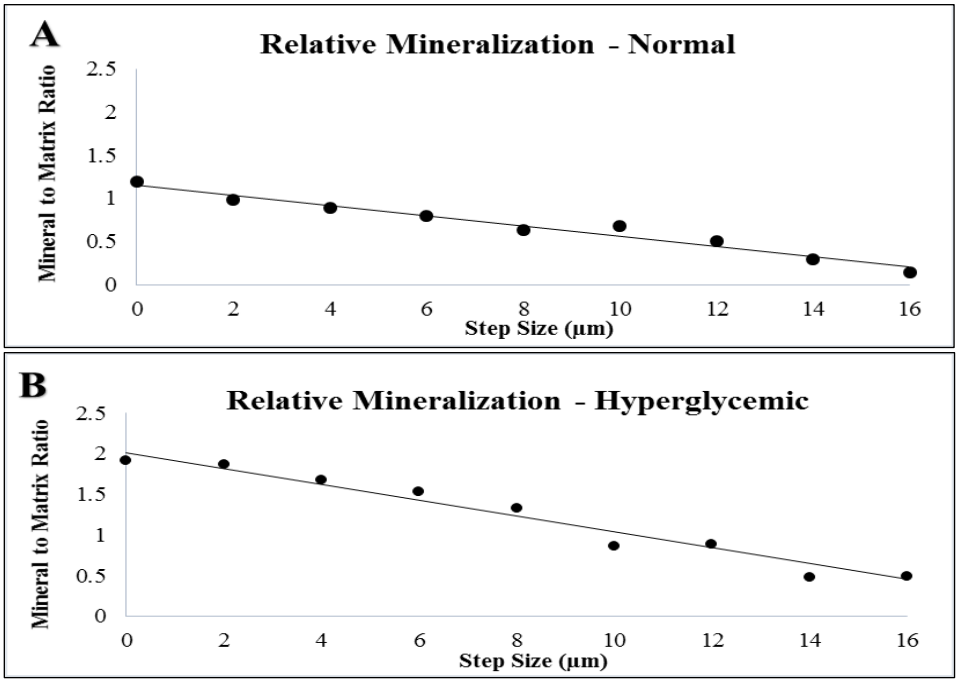

Figure 3.4 Relative Mineralization across the Mineralized Front using Raman Spectroscopy. A, B) The graphs show the mineral to matrix ratio (using the areas under the peak of PO_4^{-3} *v*1 and CH_2 wag, respectively) signal data points across the mineralized front, starting from near the center of the newly formed bone across the mineralized front, corresponding to the lines in Figure 3.3C and D. From these specific graphs, the hyperglycemic sample appeared to be more mineralized at the centre of the newly formed bone and decrease at a faster rate across the mineralized front. However, when analyzing other ROIs this trend was not observed (Figures 3.5 and 3.6).

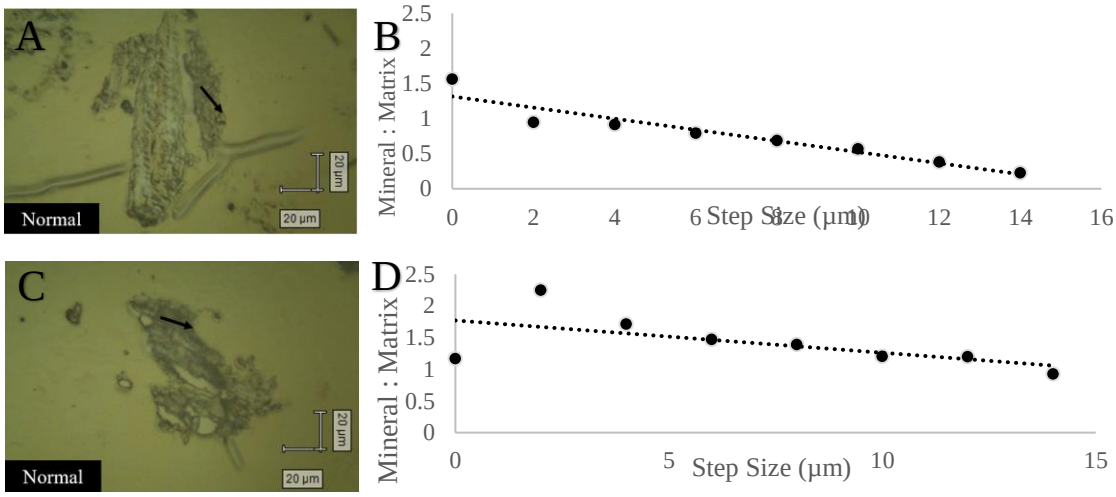

Figure 3.5 Relative Mineralization (Normal). Similar to part of Figures 3.3 and 3.4. A, C) The black arrows are ROIs where Raman line spectra were acquired from the normal sample group. B, D) The relative mineralization (using the ratio of the area under the peaks of PO_4^{-3} *v*1 to CH_2 wag) along the line spectra for the corresponding normal bone ROIs to the left (B corresponds to A and D corresponds with C).

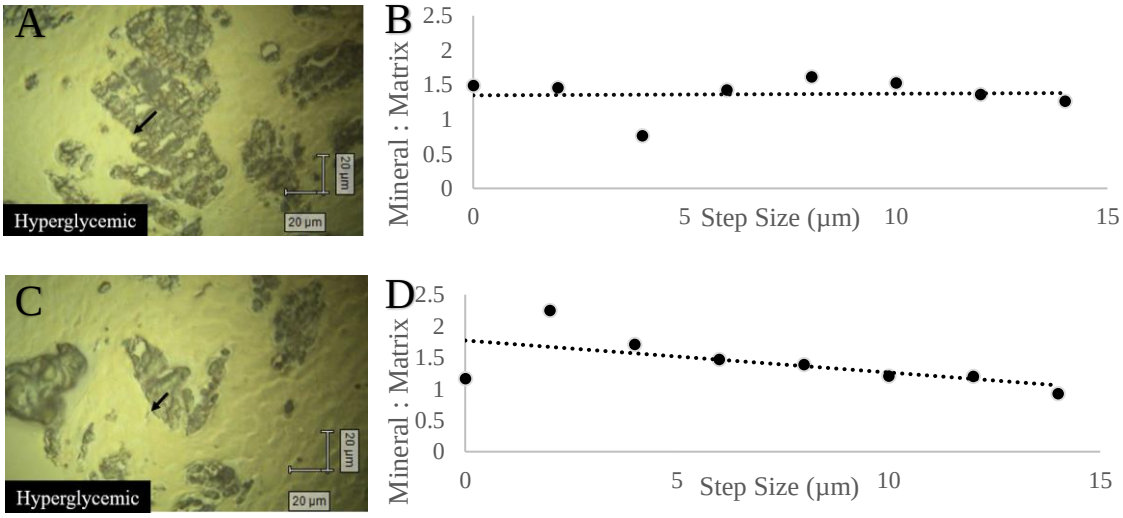

Figure 3.6 Relative Mineralization (Hyperglycemic). Similar to part of Figure 3.3 and Figure 3.4. The black arrows are ROIs where Raman line spectra were acquired from the hyperglycemic sample group. B, D) The relative mineralization (using the ratio of the area under the peaks of PO_4^{-3} *v*1 to CH_2 wag) along the line spectra for the corresponding hyperglycemic bone ROIs to the left (B corresponds to A and D corresponds with C).

Direct quantitative comparison within and between groups was difficult as the newly formed bone might differ in size and maturity. Mineralization varies in different regions of bone, with more recently deposited mineral showing less calcification than surrounding more mature regions [101]. In our experiment the regions analyzed could be anywhere from five-days old to any preceding time point since bone formation began. Therefore, it was not possible to determine which regions of the bone had been forming for the entire five-day period. With these limitations, studying the bone growth rate using Raman spectroscopy on newly formed bone, between diabetes and controls, is challenging. Most of the literature which used Raman spectroscopy to analyze bone samples has looked at mature bone [7], [102]. Raman spectroscopy can provide a micro-scale spatial resolution limited by the spot size of the laser (no less than 1μm) [103], [104]. Therefore, in order to determine if there are variations on a smaller length, scale other techniques such as TEM must be employed.

3.3 COLLAGEN-MINERAL ARRANGEMENT

With the development of high-resolution microscopy techniques, it is possible to study the nanostructure of bone. A few studies have investigated if and how the ultrastructure of diabetic bone differs from normal bone [7], [20]. However, there are still gaps in knowledge regarding the exact structural differences between diabetic and normal bone, especially in early stages of bone formation at the nanoscale [27]. TEM has briefly been used to analyze bone formation in diabetic rats in the early stages of bone growth, 10 and 21 days post-implant surgery [20]. This study showed no apparent difference in the nanostructure at the bone-implant interface at 10 days; however, they noted chondrocyte-like cells at this interface at 21 days, suggesting diabetes can alter bone formation. Despite this study showing no difference in the ultrastructure at 10 days, they

did not fully investigate the mineralization difference between the diabetic and normal sample as they decalcified their samples before TEM imaging [20].

Some researchers study the interaction between mineral and collagen after they have decalcified their samples for TEM analysis since they can study collagen morphology without the interference of the dense mineral structures [22]. In this thesis project the samples were not decalcified, which allowed a more accurate interaction between the collagen and the mineral components of bone to be studied. Research by Ajami et al. has suggested that the most significant differences in bone quality between hyperglycemic and normal individuals occur at the five-day post-implant surgery time point using micro-CT [69]. Therefore, one of the main focus points of this research was to studying if the nanostructure of bone was altered in the diabetic group at this five-day time point using high-resolution microscopy.

3.3.1 STRUCTURAL COLLAGEN-MINERAL ARRANGEMENT

The arrangement of mineral with respect to collagen fibrils on the nanoscale is commonly studied using TEM as it provides the necessary high spatial resolution. To view samples using TEM, they must be electron transparent. Two ways to prepare bone samples for TEM include FIB and ultramicrotome sectioning [92]. Ultramicrotomy is beneficial as it can prepare fairly uniform sections and is a relatively cost-efficient way to prepare bone samples for TEM. However, ultramicrotomy tends to result in artifacts from sectioning with a diamond blade, which is needed to cut through the bone samples [26], [92]. The cut of the diamond blade affects particles with different density differently. More brittle structures, such as the mineral, are likely to fragment more easily than the more flexible structures, including the collagen fibrils and the resin used to embed the bone; this could lead to distortions in the ultrastructure of bone. The diamond knife

used to ultramicrotome bone samples can also break the soft matrix leading to holes within the sample [26]. The other technique, FIB, which uses an ion beam to mill the sample, does not apply physical stress to the sample; therefore, FIB avoids many of the artifacts caused by ultramicrotomy [26]. In addition, FIB is an excellent preparation technique for TEM since it can create site-specific samples at the nano-scale. Nevertheless, FIB is limited to making small sections, approximately 10μm in width, which makes it difficult to make broad conclusions regarding a heterogeneous structure (such as woven bone) from such a small FIB section. Also, it is important to note that FIB is a very costly procedure making it less accessible to prepare numerous sections.

As the research project in this thesis was particularly interested in the mineralization patterns of newly formed bone, it was important to investigate the mineralization patterns at the mineralized front (i.e. where the most newly formed bone would be present). Therefore FIB, a site specific technique, was originally sought out to analyze the potential differences in biomineralization patterns between diabetic and normal bone formation. FIB sections were collected between the mineralized front and an osteocyte (Figure 2.6). These sections were then viewed in HAADF-STEM (Figure 3.7). In this method of imaging, brighter regions are indicative of denser elements, which can be associated with higher levels of mineralization. Figure 3.7 suggest that the normal bone is more mineralized than the hyperglycemic sample due to increased brightness of the bone. However, the FIB samples have variable thickness, which will induce variation in the contrast of the sample as well. Therefore, it is difficult to make assumptions on mineralization levels solely using visual observation. Also since these images are at high magnification and focused on the mineralized islands (MI), the less dense collagen fibrils (CF), which would presumably be present within the mineralized islands, are not clearly visible in both the normal and hyperglycemic bone sections. Also, comparing two very small FIB sections from

the disorganized woven bone and making reliable conclusions on the entire structure of the newly formed bone is challenging.

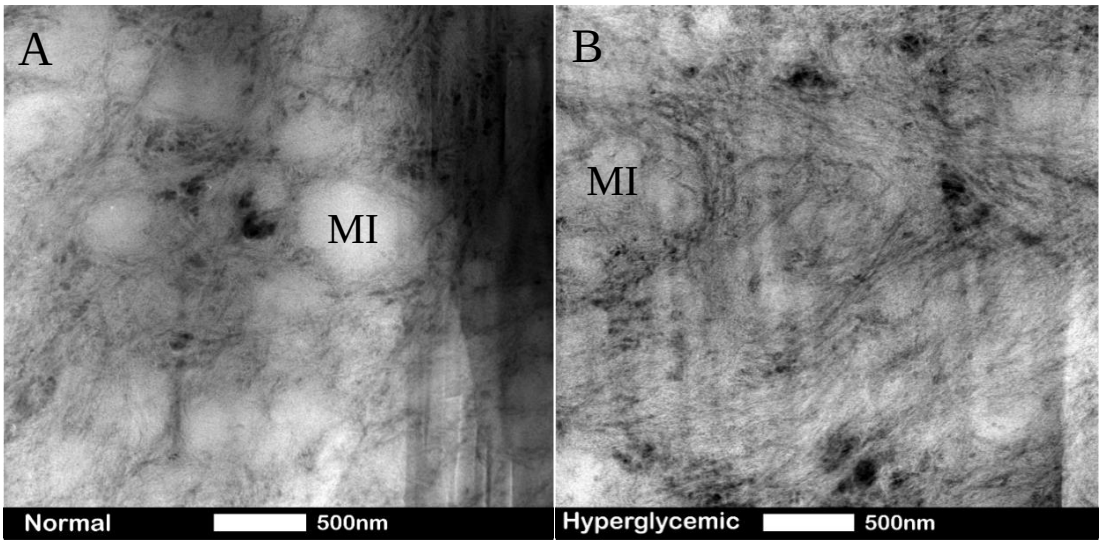

Figure 3.7 HAADF-STEM Images of Newly Formed Bone. A, B) STEM images of FIB prepared samples of the normal and hyperglycemic sections, respectively. The lighter regions are understood to be mineralized islands (MI). It appears the normal sample is slightly brighter (i.e. more mineralized) than the hyperglycemic sample.

We were also interested in observing the differences in structures across the mineralized front of woven bone between the metabolic groups. However, when the FIB lift-out method was performed there were structural discontinuities in the samples where the ROI was taken across the mineralized front (i.e. between bone and resin). It was believed that the interface between the resin and the woven bone was too delicate to retrieve a well intact FIB sample (Figure 3.8).

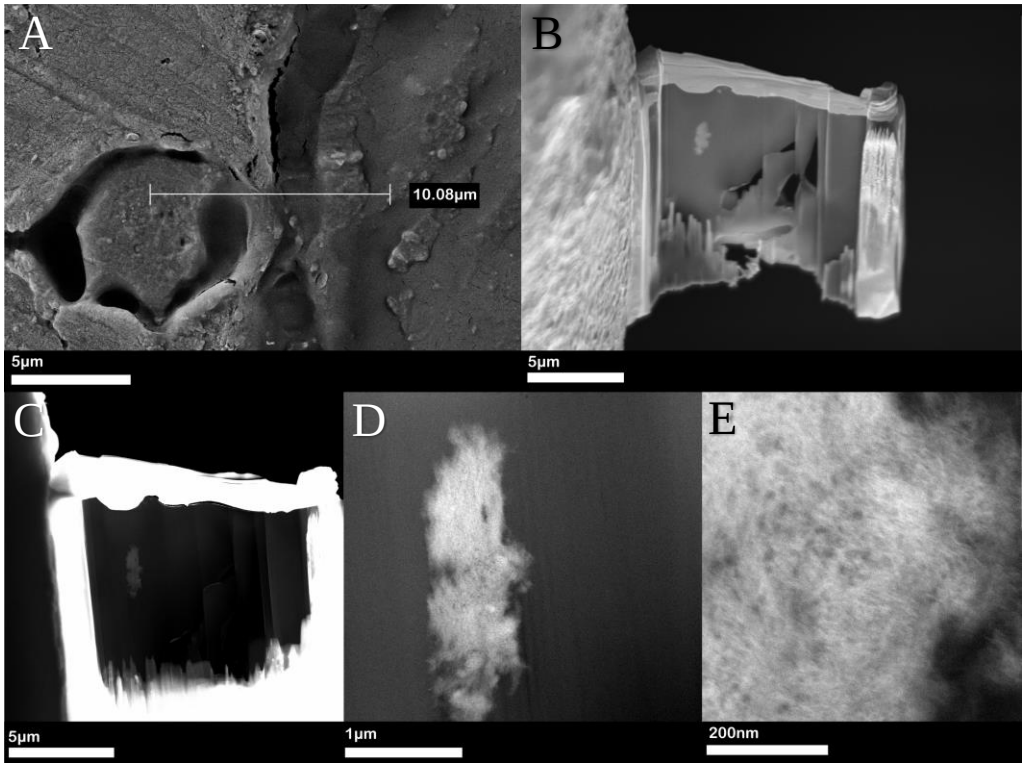

Figure 3.8 FIB Section across the Mineralized Front. A) SE SEM image of the ROI (along the line) across the mineralized front. B) SE SEM image of the FIB prepared section corresponding to the ROI to the left. C-E) Varying magnification of the FIB prepared sample viewed in STEM.

As FIB preparation made it difficult to analytically make universal conclusions between differences in the normal and hyperglycemic samples, ultramicrotomy was another TEM imaging preparation method implemented in this project. Ultramicrotomed sections with a uniform thickness of approximately 100nm were viewed under the TEM. Figure 3.9 show dark (indicative of heavier elements) globular structures, which were noted to be mineralized islands (MI), seen in early bone formation in literature [34]. It is interesting to note that in the normal sample it appeared that there were more dark structures extending into the surrounding collagen fibrils (with a characteristic banding patterns) than the hyperglycemic sample (Figure 3.9). These dark extending structures from these images were thought to exhibit intrafibrillar mineralization. However, the

images in Figure 3.9 only illustrate a small section of a heterogeneous structure and this trend was not observed when viewing other images (Figures 3.10 and 3.11).

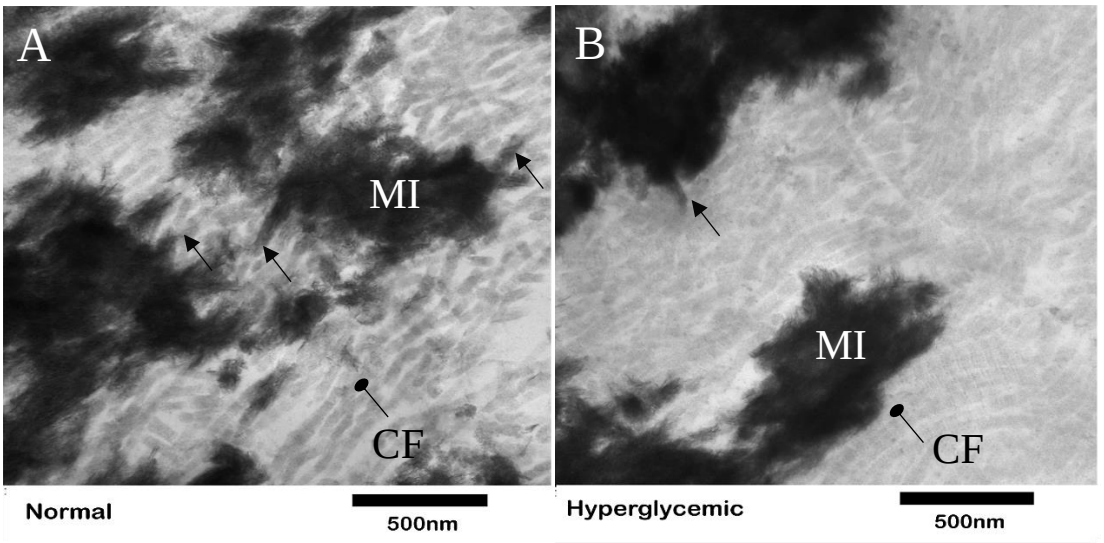

Figure 3.9 TEM BF Images of Newly Formed Bone. A, B) TEM micrographs of ultramicrotome prepared samples, for the normal and hyperglycemic sample, respectively. The oval arrow points to areas where the characteristic banding pattern of collagen fibrils (CF) can be seen. Seen in these images are mineralized islands (MI) which appears to extend into surrounding collagen fibrils, shown at regions where the black arrows are pointing towards appears to be more prevalent in the normal than the hyperglycemic samples.

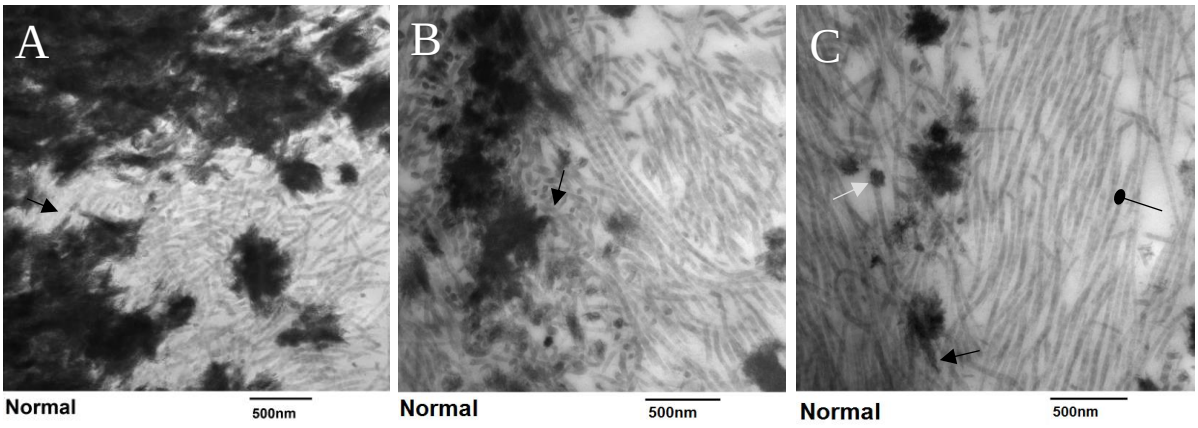

Figure 3.10 TEM BF Image of the Newly Formed Bone (Normal). Additional images of the ultramicrotome prepared samples in BF TEM for the normal group. A-B) The large dark globular structures are mineralized islands with black arrows pointing to regions extending into the surrounding collagen fibrils. C) The black oval arrows point to the characteristic banding patterns seen in collagen fibrils and the black regular arrows point to mineral extending from the mineralized areas. The white arrows point to mineralized nodules which aggregate together to form the larger mineralized islands.

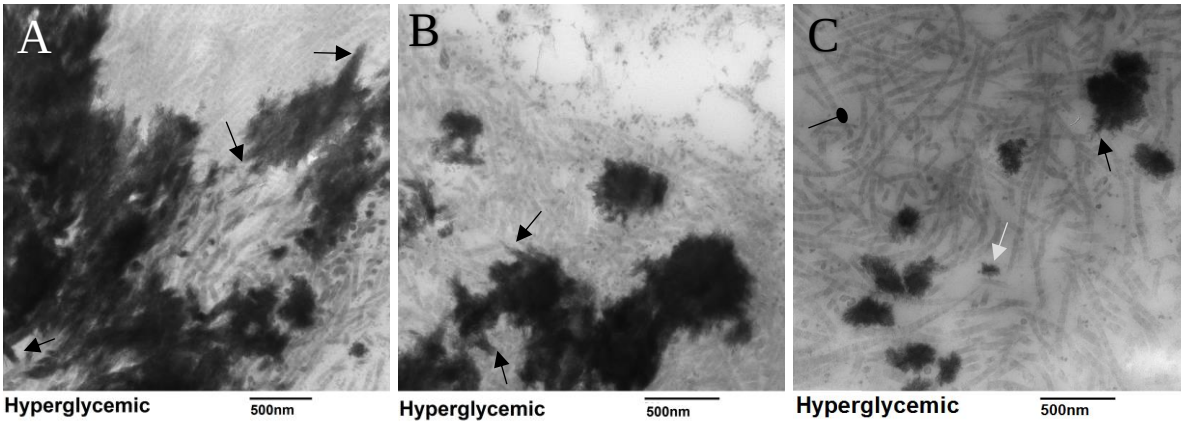

Figure 3.11 TEM Image of the Newly Formed Bone (Hyperglycemic). Additional images of the ultramicrotome prepared samples in BF TEM for the hyperglycemic group. A-B) The large dark globular structures are mineralized islands with black arrows pointing to regions extending into the surrounding collagen fibrils. C) The black oval arrows point to the characteristic banding patterns seen in collagen fibrils and the black regular arrows point to mineral extending from the mineralized areas. The white arrows point to mineralized nodules which aggregate together to form the larger mineralized islands.

Collagen morphology has been regarded as a very important factor related to biomechanical strength of tissues [15]. A previous study which investigated the diameter of decalcified collagen fibril from the femur of healthy male Wistar rats using electron microscopy measured the average diameter to be 50.4 ± 11.8 [105]. Changes in diameter and D-spacing of collagen fibrils have been speculated to be affected by mineralization levels. In particular, mineralized rat tendon collagen fibrils have shown axial contraction and lateral expansion compared to demineralized rat tendons [28]. Therefore, if hyperglycemia caused a delayed in bio-mineralization of newly formed bone, it would be expected that the hyperglycemic sample would have a smaller diameter and larger D-spacing than the normal group. Previous research, using atomic force microscopy (AFM) on rat bone, has suggested that the mean D-spacing of collagen fibrils between hyperglycemic and normal does not significantly differ in mature bone in rat specimens [7]. AFM also did not show a difference between metabolic groups in the mean D-spacing of collagen fibrils while analyzing rat tendons [7]. They did however suggest that the collagen morphology may be altered in hyperglycemic collagen fibrils, as they noted the distribution of D-spacing of collagen fibrils was greater in the hyperglycemic metabolic group than the control [7].

In our research, the average diameter and average D-spacing of the collagen fibrils were measured from the TEM BF images (Figure 3.12). The hyperglycemic collagen fibril diameters were larger than the normal group and these results were statistically significant ($p < 0.05$). The average collagen fibril diameter (from 280 measurements each) for the normal and hyperglycemic bone samples was 43.56 ± 5.53 nm and 47.70 ± 5.35 nm respectively. Although, there was no statistically significant result ($p = 0.91$) between the collagen fibril D-spacing in the metabolic groups. The average collagen fibril D-spacing for normal and hyperglycemic samples (from 160

measurements each) were 66.41 ± 4.87 nm and 66.11 ± 3.72 nm respectively. Contrary to previous research, which showed a significantly larger standard deviation of the D-spacing in the hyperglycemic sample compared to the control [7], we observed a greater standard deviation in D-spacing for the normal sample compared to the hyperglycemic.

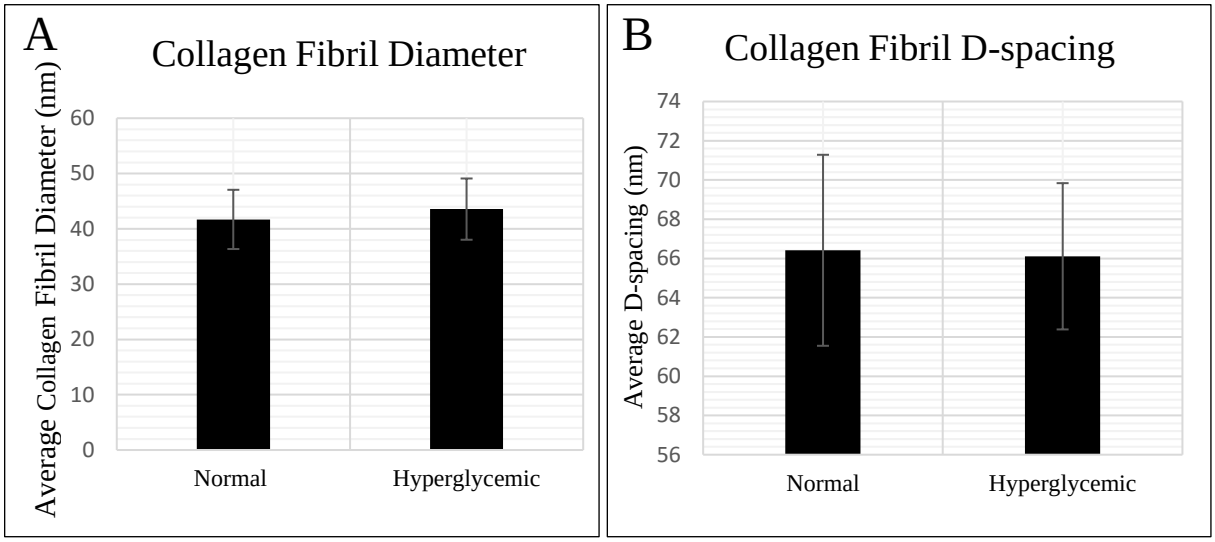

Figure 3.12 Average Collagen Fibril Measurements. A) The average diameter of 280 measurement points for each the normal and hyperglycemic sample groups. The average collagen diameter was larger for the hyperglycemic sample than the normal sample and these results were statistically significant ($p < 0.05$). B) The average D-spacing of the 160 measurement points for both the normal and hyperglycemic samples. There were no statistically significant results between the average D-spacing of the collagen fibrils for hyperglycemic and normal bone ($p > 0.05$); however, the standard deviation was greater for the normal sample than the hyperglycemic sample.

It is important to note that sample preparation and measurement techniques may cause the collagen morphology measurements to slightly differ from what would be seen *in vivo*. Since woven bone is disorganized, the collagen fibrils have different orientations with respect to one another. The collagen fibrils in our project were measured parallel to the direction of the ultramicrotome cut, as it was easiest to distinguish the collagen fibril structures. Measuring the

cross-sectional cuts of the collagen fibrils might have provided more accurate results; however, these structures could not be consistently found in the images. Moreover, even if cross-sectional fibrils were present, the fixed angle of the ultramicrotome could result in either off or perpendicular cuts creating elongated diameters. Since collagen fibrils can vary in orientation, the resultant diameter from collagen fibrils (orientated parallel to the ultramicrotome cut) can vary as well. This is due to the ultramicrotome cut having a fixed angle and possibly slicing collagen fibrils off the central axis, which would make fibrils appear smaller in diameter. Damage to collagen fibrils by the diamond knife may also distort morphology, making the diameters appear shorter. Due to the constant variability in collagen fibril orientation in woven bone, 280 data points were estimated to be enough data points to gain an average diameter.

It is also important to note that the preparation methods for electron microscopy may cause additional artifacts and sample damage in the TEM images. For electron microscopy preparation, even though the fixation in glutaraldehyde should not significantly shrink the tissue, the dehydration with ethanol can cause some shrinkage of tissue; for example, this could make the collagen fibril structure appear smaller than present *in vivo* [95]. However, since both samples were dehydrated this should not contribute to the difference between the hyperglycemic and normal samples, seen in the collagen morphology.

Therefore, the unexpected difference in collagen fibril diameter, with the collagen fibril diameter being larger in the hyperglycemic samples than the control, may be due to measurement technique. In particular, the manual measurements in ImageJ might not be as accurate as hoped. However, further investigation with different measurement techniques should be undertaken to look into these results.

3.3.2 CRYSTALLINITY

SAEDs and EDS were used to analyze the chemical composition and crystalline structures of three different ROIs including the mineralized islands, the cortical bone, and the collagen fibrils near the mineralized islands. SAEDs and EDS for multiple ROIs of the mineralized clusters for both the normal and hyperglycemic bone showed possible amorphous calcium phosphate (ACP) or nano-crystalline calcium phosphate structures, however, no preferred orientation was apparent in either sample set as expected in newly formed bone (Figures 3.13A and 3.14A). In addition to Ca and P being detected using EDS, the elements such as uranium (U) and lead (Pb) were also detected from the staining procedure and copper (Cu) was detected from the TEM grids (Figures 3.13D and 3.14D). Analysis of the cortical bone using SAEDs and EDS, for both the normal and hyperglycemic samples, showed that crystalline structures were present. Along with the corresponding images, with the c-axis of crystalline structures having a preferred orientation with the long axis of the collagen fibrils (Figures 3.13C and 3.14C), these analyses are consistent with current literature [10]. It was also noted that the collagen fibrils in both the normal and hyperglycemic bone surrounding the mineralized clusters were not mineralized (Figures 3.13B and 3.14B).

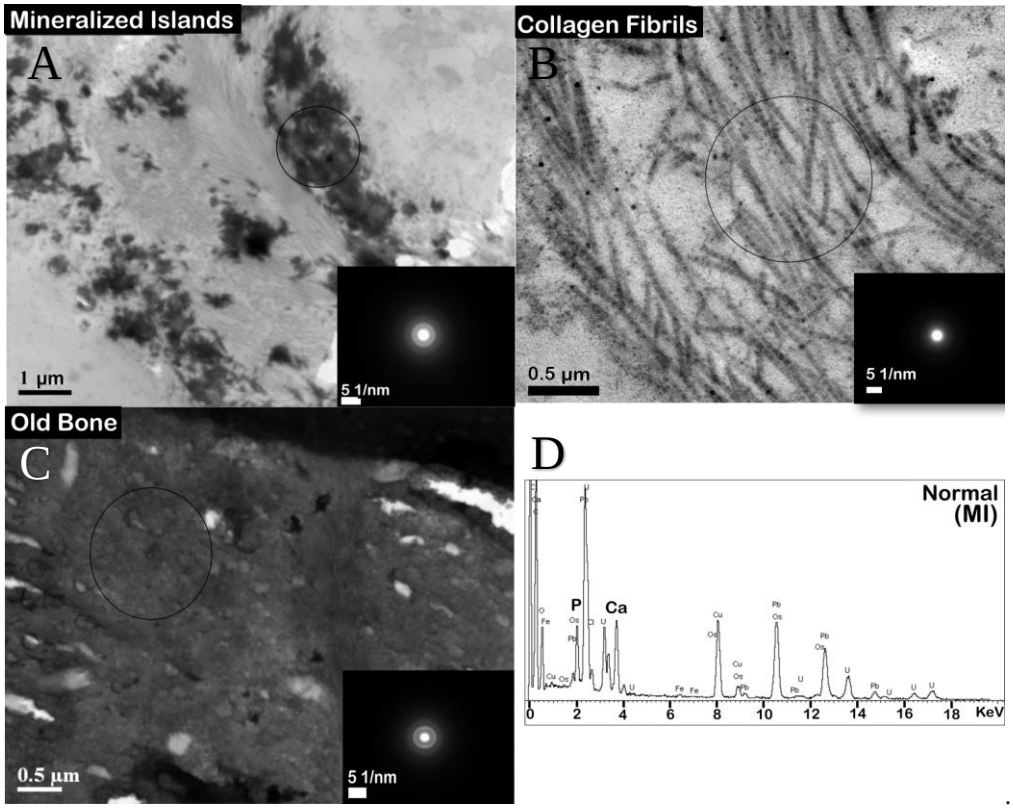

Figure 3.13 SAED and EDS for Normal Bone. A) TEM BF images of the mineralized islands with corresponding SAEDs suggesting the possibility of the presence of some amorphous or nano-crystalline structures in both the normal samples. B) Image of the collagen fibrils from the normal group near the mineralized islands illustrating no crystalline-structures. C) Region from the old bone (i.e. cortical bone) from the normal group that shows a preferred orientation of the c-axis of the crystalline structure with the long-axis of the collagen fibrils. D) EDS spectra of the mineralized islands showing Ca and P present. The stains uranyl acetate and lead citrate were also detected by EDS.

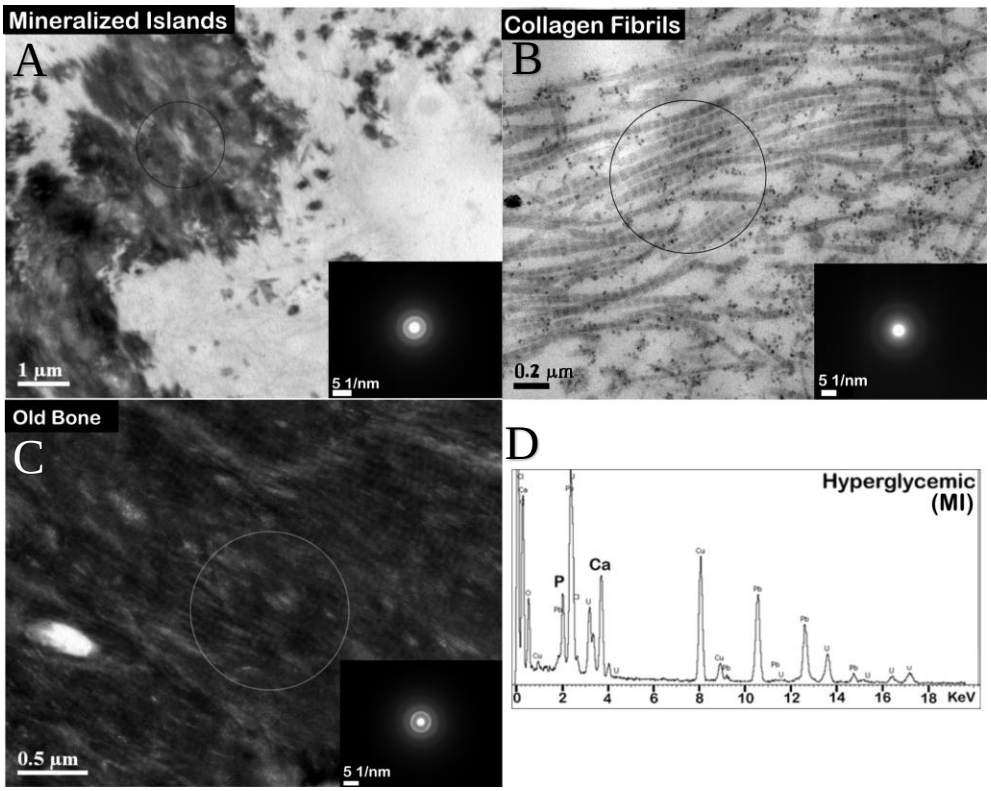

Figure 3.14 SAED and EDS for Hyperglycemic Bone. A) TEM BF images of the mineralized islands with corresponding SAED illustrating there might be amorphous or nano-crystalline structures within these structures in the hyperglycemic samples. B) SAED of collagen fibrils near the mineralized islands, showing there to no crystalline-structures in these fibrils. C) The old bone (i.e. cortical bone) from the hyperglycemic group showing a preferred orientation of the c-axis of the crystalline structure with the long-axis of the collagen fibrils. D) EDS spectra of the mineralized islands showing Ca and P present and elements from the uranyl acetate and lead citrate stain.

The quality of mineral was also studied in this thesis using Ca/P ratio from EDS data. Previous research has suggested that there is no difference in the Ca/P ratio between mature diabetic and normal bone [68]. We wanted to investigate if this ratio is altered in the hyperglycemic group in the early stages of bone growth, which may indicate altered mineral quality in hyperglycemic bone. A less mature form of crystal would be expected to have a lower Ca/P ratio [68]. The average Ca/P ratio for both the normal and hyperglycemic newly formed bone were 1.68 and 1.64, respectively (Table 3.3), similar to 1.67 Ca/P ratio of pure HA seen in literature [106].

The Ca/P ratio between the mineralized islands did not statistically significantly differ ($p = 0.73$) suggesting similar crystalline structure between the hyperglycemic and normal newly formed bone. The SAED and EDS data, along with the corresponding TEM BF images, suggest that the newly formed bone consisted of intrafibrillar and/ or interfibrillar mineralization, but the collagen fibrils near the mineralized clusters were not yet mineralized. Higher resolution investigation was needed to try to address if the mineralization of collagen fibrils surrounding mineralized islands was intrafibrillar or interfibrillar.

Table 3.3 EDS Ca/P Ratios of Mineralized Clusters. The mineralized clusters average Ca/P ratio from eight different ROIs for each metabolic group. The average Ca/P ratio was greater for the normal group than the hyperglycemic group; however, these results were not statistically significant ($p > 0.05$).

Mineralized Clusters	Normal (ROIs=8)	Hyperglycemic (ROIs=8)
Average Ca/P Ratio	1.68 ± 0.30	1.64 ± 0.20

3.3.3 BIOMINERALIZATION

Preliminary research using SEM has suggested that the delay seen in the early stages of bone growth might be due to compromised intrafibrillar mineralization rather than interfibrillar mineralization [27]. In this thesis, TEM was used to confirm if hyperglycemia causes a delay in intrafibrillar mineralization, which would suggest comprised intrafibrillar mineralization could be a contributing factor in delayed bone growth and presumably reduced bone quality seen in hyperglycemic bone compared to control groups.

Semi-quantitative information regarding the biomineralization pattern of the bone was obtained using EELS in STEM mode. EELS was used to detect the amount of mineral using the detected calcium signal, as calcium is present in mineral and not in collagen. Elemental maps were

collected from ROIs where the mineral appeared to extend out of the mineralized clusters into collagen fibrils. Figure 3.15A and B shows example ROIs of where the EELS maps were acquired in the STEM mode images. The calcium levels were then extracted from the maps. Figure 3.15C shows the amount of calcium in the corresponding ROIs in the images above, with brighter red regions illustrating more calcium. From these images (along with other EELS maps selected from different ROIs), no distinct calcium banding pattern (with a periodicity of 67 nm) was present in either sample set. This calcium banding pattern would have suggested intrafibrillar mineralization was occurring at this region.

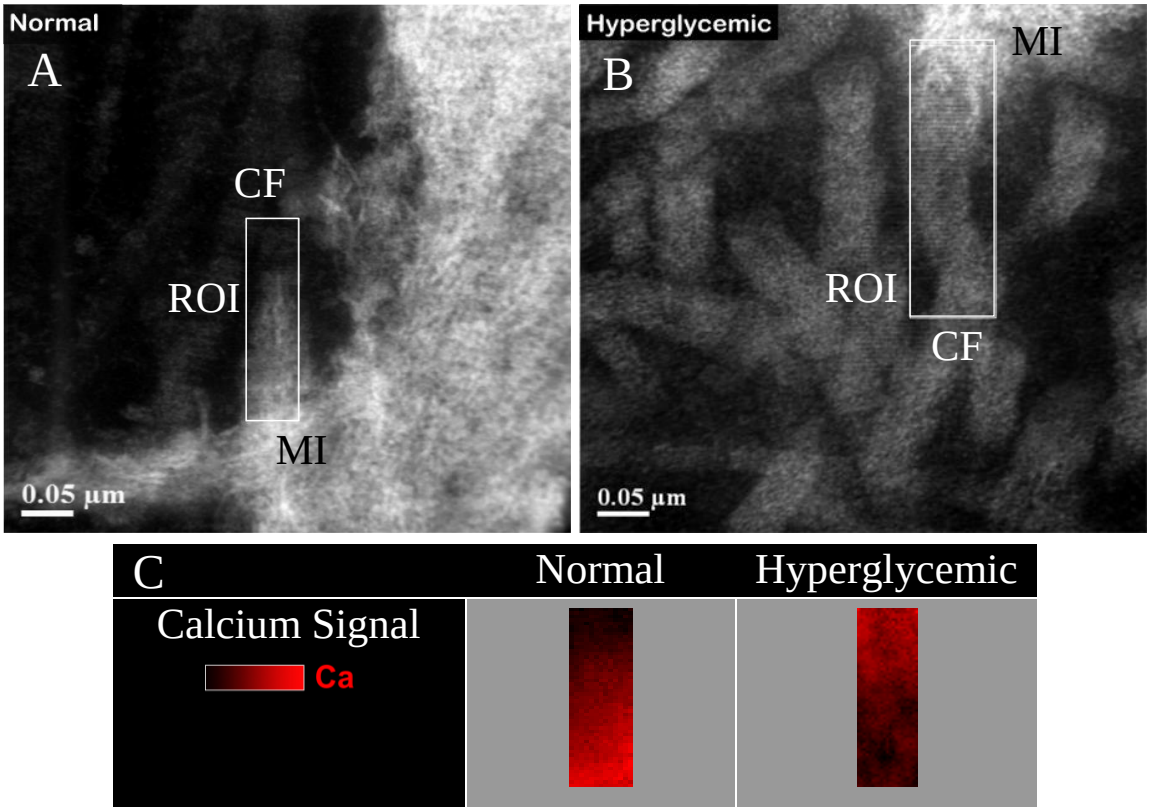

Figure 3.15 Biomineralization Pattern using EELS. A, B) STEM images of mineralized islands (MI) extending into the collagen fibrils (CF) in the normal and hyperglycemic sample respectively. C) EELS maps for calcium from corresponding ROIs above. Brighter red representing more calcium in that area.

The expected 67nm periodicity of calcium banding (with mineral laying within the gap zones) was not present in either the normal or hyperglycemic group via TEM images and EELS. Therefore, these EELS results suggest there is no difference in the mineralization between the normal and hyperglycemic groups. However, since 3D structures are represented in a 2D image using TEM, issues with the depth perception when analyzing the 2D TEM micrographs might account for the observation that there is no difference in mineralization patterns. For example, when determining whether calcium was present inside the collagen fibril, the mineral may be laying on top of the collagen fibril rather than within and with these 2D imaging techniques this cannot be determined. This might mean that interfibrillar mineralization occurred in these regions (i.e. the mineral laying between collagen fibrils). If interfibrillar mineralization occurred, it might be difficult to detect intrafibrillar mineralization in the same regions via imaging. These technical limitations make it difficult to conclude with certainty that intrafibrillar mineralization is not delayed in hyperglycemic bone.

CHAPTER 4

CONCLUSIONS

4.1 SUMMARY OF MAJOR FINDINGS

The research presented in this thesis investigated compromised bone healing seen in hyperglycemic compared to normal (i.e. control) groups by analyzing various indicators of bone quality including bone porosity, relative mineralization level, crystallinity, collagen and mineral arrangement, and collagen morphology.

Bone porosity, an indicator of bone quality, was analyzed using micro-CT, a 1-2 μm resolution 3D imaging modality, and SEM, a higher resolution 2D imaging technique. No significant difference in new bone porosity was observed between the hyperglycemic and the normal samples using SEM; however, an increased porosity was seen in the hyperglycemic samples compared to the normal samples using micro-CT. These results suggest that the hyperglycemic sample was more porous than the normal sample when the larger porous structures that would not appear in the 2D SEM images appeared in the micro-CT. These results suggest that at the five-day time point, the higher porosity seen in the hyperglycemic new bone formation compared to the normal bone might be contributing to the increased implant failure seen in literature in individuals with uncontrolled or misdiagnosed diabetes.

The degree of mineralization, another indicator of bone quality, measured by Raman spectroscopy did not appear to differ between the hyperglycemic and normal groups across the mineralized front of bone. In both sample groups, the mineralization level, measured by the ratio of PO_4^{-3} v1 to CH_2 wag, decreased towards the mineralized front. However, making a direct comparison in the relative mineralization (within and between metabolic groups) proved to be

difficult as different ROIs within the same sample could vary in maturity levels due to the disorganized structure of the woven (i.e. newly formed) bone.

Collagen fibril morphology significantly differed between the hyperglycemic and control group in the average diameter of the collagen fibril but no significant result was observed in the average D-spacing of the collagen fibrils between metabolic groups. These results did not align with the hypothesis going into this research. It was hypothesized that the hyperglycemic sample would be less mineralized than the normal sample, resulting in the hyperglycemic sample having a smaller diameter and larger D-spacing of collagen fibrils compared to control groups. However, these finding might be a result of limitations associated with ultramicrotoming woven bone, and further work is needed to investigate this observation.

The TEM analysis of the ultrastructure and crystallinity of the cortical bone, newly formed woven bone, and collagen fibrils appeared to be similar for both the normal and hyperglycemic samples. While diffraction patterns of older bone showed oriented crystals along the c-axis of the collagen fibrils, newly formed woven bone contained mostly amorphous or nano-crystalline structures, and the collagen fibrils surrounding the cluster had no detectable mineral. This indicates at the five-day time point of bone healing, the bone in both the hyperglycemic and normal groups are composed mainly of collagen rich osteoid and mineralized islands. A similar Ca/P ratio was detected by EDS in the mineralized islands in both metabolic groups, which confirmed that hydroxyapatite was present in these regions. Highly organized mineralized collagen fibrils, seen in mature bone, were not seen in abundance at the five-day time point.

Elemental analysis of biomineralization was done using EELS. The calcium signals, representative of the mineral content, detected in EELS appeared to be similar between the normal

and hyperglycemic group, suggesting that a disruption in intrafibrillar mineralization may not necessarily be the reason for delayed bone growth in hyperglycemia at the five-day time point.

In summary, it is suggested that the altered micro-architecture (i.e. porosity) rather than the nano-architecture (i.e. the collagen-mineral arrangement) might be a major contributing factor to the increased implant failure rate in uncontrolled or misdiagnosed diabetes reported in literature. We propose that the five-day time point of bone healing might be too early to detect any ultrastructure changes within diabetic bone which may contribute to its delayed bone formation seen in literature. Table 4.1 provides an overview of the results obtained from this thesis project.

Table 4.1 Assessment of Bone Quality. An overview of the variables measured to assess bone quality in hyperglycemic compared to normal groups with the corresponding techniques used and the outcomes of the experiment.

Variable	Techniques	Results of this thesis
Bone Microarchitecture	Micro-CT	The 3D porosity of the hyperglycemic group was significantly larger than normal group.
	SEM	The 2D porosity between metabolic groups did not differ.
Matrix/Mineral Composition	Raman Spectroscopy	Similar trends were observed in relative mineralization across mineralized front for both hyperglycemic and normal samples.
Bone Nanoarchitecture	TEM STEM	There was no apparent difference in the arrangement of collagen and mineral between metabolic groups.
Crystallinity	SAED	For both the metabolic groups, the newly formed bone appeared to have amorphous or nano-crystalline structures.
	EDS	The newly formed bone from both the hyperglycemic group and normal group had similar Ca/P ratios.
Biomineralization	STEM EELS	No delay in intrafibrillar mineralization in the hyperglycemic group compared to the normal group was observed.

4.2 LIMITATIONS AND FUTURE STUDIES

In addition to the difficulty in analyzing woven bone using the microscopy techniques mentioned throughout the thesis, it is important to note that this research project was a pilot study, meaning only a small sample size was available for this study. Also, it is important to note there is no perfect animal model to replicate human conditions. Due to ethical reasons, it would be unreasonable to replicate this experiment, which required surgical intervention and harvesting bone for studies high-resolution microscopy techniques, in humans. While the STZ-induced rat model is one of the most common animal models to study experimental diabetes, it resembles T1DM in humans rather than the more common T2DM seen in humans [81]. Therefore, the conclusions drawn from this experiment may not be fully representative of biological processes that are occurring in the human population. It is also important to note that the bone microstructure of rats differs from humans as rats do not have secondary osteons, which is one of the arrangements of lamellae in human cortical bone [107] (Figure 1.1).

Rodents, such as rats and mice, are commonly used to study diabetes [81]. However, other animals which resemble humans more closely are needed to mimic more clinical situations [108]. Other common animal models used in bone-implant research include the dog, pig, sheep, goat, and rabbit models [109]. When selecting an animal model (for bone research) it is important to take into consideration factors such as the cost to purchase and care for the animals, acceptability to society, and the animal similarity (bone macrostructure, microstructure, and composition) to humans [109]. With these factors considered we propose that pigs may be a better model to study bone, as pigs are considered closely related to humans with respect to bone anatomy, morphology, healing, microstructure, bone composition, and remodelling [109]. Pigs models have already begun to be used in diabetic research [71], [108], [110].

Future studies are needed to analyze more time points in the bone healing process. In particular, a time point study at 7 days, 14 days, 21 days, and 28 days post-surgery similar to other studies which suggested and/or identified differences in bone growth [20], [69], [96]. In addition, if novel results are found, a larger sample size should be investigated. With regards to techniques used to investigate bone, it might also be interesting to use electron tomography to get a 3D high-resolution visualization to better analyze the nano-structural difference between the hyperglycemic samples. Even though we did not see a difference in the nanostructure between hyperglycemic and normal bone, this lack of difference may be due to the 2D imaging limitations associated with the TEM methods employed in this work. Therefore, further work is needed to investigate the effects of hyperglycemia on bone quality in the early stages of bone formation.

REFERENCES

[1] U. G. K. Wegst, H. Bai, E. Saiz, A. P. Tomsia, R. O. Ritchie, C. Ortiz, M. Boyce, U. G. K. Wegst, H. Bai, E. Saiz, A. P. Tomsia, and R. O. Ritchie, "Bioinspired structural materials," *Nat. Mater.*, vol. 14, no. 1, pp. 23–36, 2014.

[2] K. Grandfield, A. Palmquist, and H. Engqvist, "High-resolution three-dimensional probes of biomaterials and their interfaces," *Philos. Trans. R. Soc. A Math. Phys. Eng. Sci.*, vol. 370, pp. 1337–1351, 2012.

[3] W. Landis, M. Song, A. Leith, L. McEwen, and B. McEwen, "Mineral and Organic Matrix Interaction in Normally Calcifying Tendon Visualized in Three Dimension by High-Voltage Electron Microscopic Tomography and Graphic Image Reconstruction," *J. Struct. Biol.*, pp. 39–54, 1993.

[4] E. McNally, H. Schwarcz, G. Botton, and A. Arsenault, "A model for the ultrastructure of bone based on electron microscopy of ion-milled sections," *PLoS One*, vol. 7, no. 1, p. e29258, 2012.

[5] X. Su, K. Sun, F. Cui, and W. Landis, "Organization of apatite crystals in human woven bone," *Bone*, vol. 32, no. 2, pp. 150–162, 2003.

[6] K. Vernon-Parry, "Scanning Electron Microscopy: an introduction," *III-Vs Rev.*, vol. 13, no. 4, pp. 40–44, 2000.

[7] M. Hammond, M. Gallant, D. Burr, and J. Wallace, "Nanoscale changes in collagen are reflected in physical and mechanical properties of bone at the microscale in diabetic rats," *Bone*, vol. 60, pp. 26–32, 2014.

[8] M. Olszta, X. Cheng, S. Jee, R. Kumar, Y.-Y. Kim, M. Kaufman, E. Douglas, and L.

Gower, “Bone structure and formation: A new perspective,” *Mater. Sci. Eng. R Reports*, vol. 58, no. 3–5, pp. 77–116, 2007.

[9] A. Arsenault, “Ultrastructure of Skeletal Tissue,” in *Ultrastructure of Skeletal Tissues: Bone and Cartilage in Health Disease*, E. Bonucci and P. Motta, Eds. Springer US, 1990, p. 5.

[10] N. Reznikov, R. Shahar, and S. Weiner, “Bone hierarchical structure in three dimensions,” *Acta Biomater.*, vol. 10, no. 9, pp. 3815–26, 2014.

[11] B. Clarke, “Normal Bone Anatomy and Physiology,” *Clin. J. Am. Soc. Nephrol.*, vol. 3, pp. S131–S139, 2008.

[12] M. Doblaré, J. M. García, and M. J. Gómez, “Modelling bone tissue fracture and healing: A review,” *Eng. Fract. Mech.*, vol. 71, no. 13–14, pp. 1809–1840, 2004.

[13] S. Weiner, W. Traub, and H. D. Wagner, “Lamellar Bone : Structure – Function Relations,” vol. 255, pp. 241–255, 1999.

[14] E. Donnelly, “Methods for assessing bone quality: A review,” *Clin. Orthop. Relat. Res.*, vol. 469, no. 8, pp. 2128–2138, 2011.

[15] M. Tzaphlidou, “Bone architecture: Collagen Structure and Calcium/Phosphorus Maps,” *J. Biol. Phys.*, vol. 34, pp. 39–49, 2008.

[16] A. Milczarczyk and E. Franek, “Osteoporosis and bone fractures in patients with diabetes mellitus,” *Diabetol. Dosw. i Klin.*, pp. 63–67, 2008.

[17] J. N. Farr and S. Khosla, “Determinants of bone strength and quality in diabetes mellitus in humans,” *Bone*, vol. 82, pp. 28–34, 2016.

[18] M. Ruppel, L. Miller, and D. Burr, “The effect of the microscopic and nanoscale structure

on bone fragility," *Osteoporos. Int.*, pp. 1251–1265, 2008.

[19] S. Viguet-Carrin, P. Garnero, and P. Delmas, "The role of collagen in bone strength," *Osteoporos. Int.*, vol. 17, no. 3, pp. 319–336, 2006.

[20] J. Siqueira, S. Cavalher-Machado, V. Arana-Chavez, and P. Sannomiya, "Bone Formation Around Titanium Implants in the Rat Tibia: Role of Insulin," *Implant Dent.*, vol. 12, pp. 242–251, 2003.

[21] C. Rey, C. Combes, C. Drouet1, and M. Glimcher, "Bone mineral: update on chemical composition and structure," *Osteoporos. Int.*, vol. 20, no. June 2008, pp. 1013–1021, 2010.

[22] B. Wopenka and J. Pasteris, "A mineralogical perspective on the apatite in bone," *Mater. Sci. Eng. C*, vol. 25, no. 2, pp. 131–143, 2005.

[23] J. Petruska and A. Hodge, "A Subunit Model For The Tropocollagen Macromolecule," *Proc. Natl. Acad. Sci. U. S. A.*, vol. 51, pp. 871–876, 1964.

[24] E. McNally, F. Nan, G. Botton, and H. Schwarcz, "Scanning transmission electron microscopic tomography of cortical bone using Z-contrast imaging," *Micron*, vol. 49, pp. 46–53, 2013.

[25] B. Alexander, T. L. Daulton, G. M. Genin, J. Lipner, J. D. Pasteris, B. Wopenka, and S. Thomopoulos, "The nanometre-scale physiology of bone: steric modelling and scanning transmission electron microscopy of collagen-mineral structure," *J. R. Soc. Interface*, vol. 9, no. 73, pp. 1774–1786, 2012.

[26] H. Schwarcz, "The ultrastructure of bone as revealed in electron microscopy of ion-milled sections," *Semin. Cell Dev. Biol.*, vol. 46, pp. 44–50, 2015.

[27] E. Ajami, S. Bell, R. Liddell, and J. Davies, “Early Bone Anchorage to Micro- and Nano-topographically Complex Implant Surfaces in Hyperglycemia,” *Acta Biomater.*, pp. 1–11, 2016.

[28] B. Quan and E. Sone, “Structural changes in collagen fibrils across a mineralized interface revealed by cryo-TEM,” *Bone*, vol. 77, pp. 42–49, 2015.

[29] F. F. Safadi, M. F. Barbe, S. M. Abdelmagid, M. C. Rico, R. A. Aswad, J. Litvin, and S. N. Popoff, *Bone Pathology*, vol. 2. Totowa, NJ: Humana Press, 2009.

[30] R. Dimitriou, E. Tsiridis, and P. Giannoudis, “Current concepts of molecular aspects of bone healing,” *Injury*, vol. 36, no. 12, pp. 1392–1404, 2005.

[31] A. Robling, A. Castillo, and C. Turner, “Biomechanical and Molecular Regulation of Bone Remodeling,” *Annu. Rev. Biomed. Eng.*, vol. 8, no. 1, pp. 455–498, 2006.

[32] K. Paiva and J. Granjeiro, “Bone tissue remodeling and development: Focus on Matrix metalloproteinase functions,” *Arch. Biochem. Biophys.*, 2014.

[33] J. Glowacki, “Angiogenesis in fracture repair.,” *Clin. Orthop. Relat. Res.*, no. 355 Suppl, pp. S82–9, 1998.

[34] J. Davies and M. Hosseini, “Histodynamics of Endosseous Wound Healing,” *Bone Eng.*, no. January, pp. 1–14, 2000.

[35] S. Guo and L. Dipietro, “Factors affecting wound healing,” *J. Dent. Res.*, vol. 89, no. 3, pp. 219–229, 2010.

[36] M. Retzepi and N. Donos, “The effect of diabetes mellitus on osseous healing,” *Clin. Oral Implants Res.*, vol. 21, no. 7, pp. 673–681, 2010.

[37] R. Carano and E. Filvaroff, “Angiogenesis and bone repair,” *Drug Discov. Today*, vol. 8,

no. 21, pp. 980–989, 2003.

[38] N. Reznikov, R. Shahar, and S. Weiner, “Three-dimensional structure of human lamellar bone: the presence of two different materials and new insights into the hierarchical organization,” *Bone*, vol. 59, pp. 93–104, 2014.

[39] E. Bonucci, “The Mineralization of Bone and Its Analogies with Other Hard Tissues,” in *Advanced Topics on Crystal Growth*, S. Ferreira, Ed. InTech, 2013, pp. 145–184.

[40] G. Bernard, “The ultrastructural interface of bone crystals and organic matrix in woven and lamellar endochondral bone,” *J. Dent. Res.*, vol. 48, no. 5, pp. 781–788, 1969.

[41] D. Cameron, “The Fine structure of bone and calcified cartilage,” *Clin Orthop Relat Res.*, vol. 26. pp. 199–228, 1963.

[42] S. Jackson, “The fine structure of developing bone in embryonic fowl,” *R. Soc. London. Ser. B, Biol. Sci.*, 1956.

[43] M. J. Glimcher, “Molecular Biology of Mineralized Tissues with Particular Reference to Bone,” *Rev. Mod. Phys.*, vol. 31, no. 2, pp. 359–393, 1959.

[44] J. Sela and I. Bab, “The Relationship Between Extracellular Matrix Vesicles and Calcospherities in Primary Mineralization of Neoplastic Bone Tissue,” *Virchows Arch. A. Pathol. Anat. Histol.*, vol. 382, no. 1, pp. 1–9, 1979.

[45] L. Martino, V. Yeager, and J. Taylor, “An Ultrastructural Study of the Role of Calcification Nodules in the Mineralization of Woven Bone,” *Calcif. Tissue Int.*, vol. 27, pp. 57–64, 1979.

[46] H. Ozawa, K. Hoshi, and N. Amizuka, “Current Concepts of Bone Biomineralization,” *J. Oral Biosci.*, vol. 50, no. 1, pp. 1–14, 2008.

[47] D. Damasceno, A. Netto, I. Iessi, F. Gallego, S. Corvino, and B. Dallaqua, "Streptozotocin-Induced Diabetes Models: Pathophysiological Mechanisms and Fetal Outcomes," *Biomed Res. Int.*, vol. 1, pp. 1–11, 2014.

[48] "IDF Diabetes Atlas Sixth Edition." International Diabetes Federation, 2014.

[49] L. McCabe, "The Diabetes-Bone Relationship," *J. Diabetes Metab.*, vol. 01, no. S1, pp. 1–2, 2012.

[50] F. Javed and G. Romanos, "Impact of Diabetes Mellitus and Glycemic Control on the Osseointegration of Dental Implants: A Systematic Literature Review," *J. Periodontol.*, vol. 80, no. 11, pp. 1719–1730, 2009.

[51] A. M. Inzerillo and S. Epstein, "Osteoporosis and diabetes mellitus," *Rev. Endocr. Metab. Disord.*, vol. 5, no. 3, pp. 261–268, 2004.

[52] V. Zhukouskaya, A. Shepelkevich, and I. Chiodini, "Bone Health in Type 1 Diabetes: Where We Are Now and How We Should Proceed," *Adv. Endocrinol.*, vol. 2014, pp. 1–12, 2014.

[53] P. Vestergaard, "Discrepancies in bone mineral density and fracture risk in patients with type 1 and type 2 diabetes - A meta-analysis," *Osteoporos. Int.*, vol. 18, no. 4, pp. 427–444, 2007.

[54] E. Gorman, A. Chudyk, K. Madden, and M. Ashe, "Bone health and type 2 diabetes mellitus: A systematic review," *Physiother. Canada*, vol. 63, no. 1, pp. 8–20, 2011.

[55] M. Saito and K. Marumo, "Bone quality in diabetes," *Front. Endocrinol. (Lausanne).*, vol. 4, no. June, pp. 1–9, 2013.

[56] L. Hofbauer, C. Brueck, S. Singh, and H. Dobnig, "Osteoporosis in Patients with Diabetes

Mellitus," *J. Bone Miner. Res.*, vol. 22, no. 9, pp. 1317–1328, 2007.

[57] C. Hamann, C. Goettsch, J. Mettelsiefen, V. Henkenjohann, M. Rauner, U. Hempel, R. Bernhardt, N. Fratzl-Zelman, P. Roschger, S. Rammelt, K. Gunther, and L. Hofbauer, "Delayed bone regeneration and low bone mass in a rat model of insulin-resistant type 2 diabetes mellitus is due to impaired osteoblast function," *AJP Endocrinol. Metab.*, vol. 301, no. 17, pp. E1220–E1228, 2011.

[58] J. Paccou, K. Ward, K. Jameson, E. Dennison, C. Cooper, and M. Edwards, "Bone Microarchitecture in Men and Women with Diabetes: The Importance of Cortical Porosity," *Calcif. Tissue Int.*, vol. 98, no. 5, pp. 465–473, 2016.

[59] M. Rubin and J. Patsch, "Assessment of bone turnover and bone quality in type 2 diabetic bone disease: current concepts and future directions," *Bone Res.*, vol. 4, no. November 2015, p. 16001, 2016.

[60] A. Picke, I. Gordaliza Alaguero, G. Campbell, C. Glüer, J. Salbach-Hirsch, M. Rauner, L. Hofbauer, and C. Hofbauer, "Bone defect regeneration and cortical bone parameters of type 2 diabetic rats are improved by insulin therapy," *Bone*, vol. 82, pp. 4–11, 2015.

[61] A. Shu, M. Yin, E. Stein, S. Cremers, E. Dworakowski, R. Ives, and M. Rubin, "Bone structure and turnover in type 2 diabetes mellitus," *Osteoporos. Int.*, vol. 23, no. 2, pp. 635–641, 2012.

[62] J. Farr, M. Drake, S. Amin, L. Melton, L. McCready, and S. Khosla, "In Vivo Assessment of Bone Quality in Postmenopausal Women with Type 2 Diabetes," *J. Bone Miner. Res.*, vol. 29, no. 4, pp. 784–786, 2014.

[63] Y. Bala, D. Farlay, and G. Boivin, "Bone mineralization: From tissue to crystal in normal

and pathological contexts," *Osteoporos. Int.*, vol. 24, no. 8, pp. 2153–2166, 2013.

[64] D. Facchini, V. Yuen, M. Battell, J. McNeill, and M. Grynpas, "The effects of vanadium treatment on bone in diabetic and non-diabetic rats," *Bone*, vol. 38, no. 3, pp. 368–377, 2006.

[65] D. Farlay, L. Armas, E. Gineyts, M. Akhter, R. Recker, and G. Boivin, "Nonenzymatic Glycation and Degree of Mineralization Are Higher in Bone from Fractured Patients with Type 1 Diabetes Mellitus," *J. Bone Miner. Res.*, vol. 31, no. 1, pp. 190–195, 2016.

[66] K. Fulzele, R. Riddle, D. DiGirolamo, X. Cao, C. Wan, D. Chen, M.-C. Faugere, S. Aja, M. Hussain, J. Bruning, and T. Clemens, "Insulin Receptor Signaling in Osteoblasts Regulates Postnatal Bone Acquisition and Body Composition," *Cell*, vol. 142, no. 2, pp. 309–319, 2010.

[67] S. Hough, L. Avioli, M. Bergfeld, D. Michael, E. Slatopolsky, and S. Teitelbaum, "Correction of Abnormal Bone and Mineral Metabolism in Chronic Streptozotocin-Induced Diabetes Mellitus in the Rat by Insulin Therapy," vol. 108, no. 6, pp. 2228–2234, 1981.

[68] T. Einhorn, A. Boskey, C. Gundberg, V. Vigorita, V. Devlin, and M. Beyer, "The mineral and mechanical properties of bone in chronic experimental diabetes.," *J. Orthop. Res.*, vol. 6, no. 3, pp. 317–23, 1988.

[69] E. Ajami, E. Mahno, V. C. Mendes, S. Bell, R. Moineddin, and J. E. Davies, "Bone healing and the effect of implant surface topography on osteoconduction in hyperglycemia.," *Acta Biomater.*, vol. 10, no. 1, pp. 394–405, 2014.

[70] S. Mehta, E. Breitbart, W. Berberian, F. Liporace, and S. Lin, "Bone and Wound Healing

in the Diabetic Patient," *Foot Ankle Clin.*, vol. 15, no. 3, pp. 411–437, 2010.

[71] P. Velander, C. Theopold, T. Hirsch, O. Bleiziffer, B. Zuhaili, M. Fossum, D. Hoeller, R. Gheerardyn, M. Chen, S. Visovatti, H. Svensson, F. Yao, and E. Eriksson, "Impaired wound healing in an acute diabetic pig model and the effects of local hyperglycemia," *Wound Repair Regen.*, vol. 16, no. 2, pp. 288–293, 2008.

[72] H. Brem and M. Tomic-Canic, "Cellular and molecular basis of wound healing in diabetes," *J. Clin. Invest.*, vol. 117, no. 5, pp. 1219–1222, 2007.

[73] R. Santana, L. Xu, H. Chase, S. Amar, D. Graves, and P. Trackman, "A Role for Advanced Glycation End Products in Diminished Bone Healing in Type 1 Diabetes," *Diabetes*, vol. 52, no. August 2002, pp. 1502–1510, 2003.

[74] D. Graves, J. Alblowi, D. Paglia, J. O'Connor, and S. Lin, "Impact of Diabetes on Fracture Healing," *J. Exp. Clin. Med.*, vol. 3, no. 1, pp. 3–8, 2011.

[75] H. Naujokat, B. Kunzendorf, and J. Wiltfang, "Dental implants and diabetes mellitus - a systematic review," *Int. J. Implant Dent.*, vol. 2, no. 1, p. 5, 2016.

[76] J. Porter and J. Von Fraunhofer, "Success or failure of dental implants? A literature review with treatment considerations," *Gen. Dent.*, vol. 53, no. 6, pp. 423–432, 2005.

[77] T. Albrektsson and C. Johansson, "Osteoinduction, osteoconduction and osseointegration," *Eur. Spine J.*, vol. 10, pp. 96–101, 2001.

[78] E. Mahno, "Bone Healing in Diabetes Mellitus Associated Hyperglycemia by Bone Healing in Diabetes Mellitus Associated Hyperglycemia," University of Toronto, 2010.

[79] M. Giglio, G. Giannunzio, D. Olmedo, and M. Guglielmotti, "Histomorphometric Study of Bone Healing Around Laminar Implants in Experimental Diabetes," *Implant dentistry*,

vol. 9, no. 2. pp. 143–149, 2000.

[80] N. Follak, I. Klöting, E. Wolf, and H. Merk, “Delayed remodelling in the early period of fracture healing in spontaneously diabetic BB/OK rats depending on the diabetic metabolic state,” *Histol. Histopathol.*, vol. 19, no. 2, pp. 473–486, 2004.

[81] A. King, “The use of animal models in diabetes research,” *Br. J. Pharmacol.*, vol. 166, no. 3, pp. 877–894, 2012.

[82] A. Akbarzadeh, D. Norouzian, M. Mehrabi, S. Jamshidi, A. Farhangi, A. Allah Verdi, S. Mofidian, and B. Lame Rad, “Induction of Diabetes by Streptozotocin in Rats,” *Indian J. Clin. Biochem.*, vol. 22, no. 2, pp. 60–64, 2007.

[83] “Definition and Diagnosis of Diabetes Mellitus and Intermediate Hyperglycemia.” World Health Organization, p. 50, 2006.

[84] K. Motyl and L. Mccabe, “Streptozotocin , Type I Diabetes Severity and Bone,” *Biol. Proced. Online*, vol. 11, no. 1, pp. 296–315, 2009.

[85] M. Klein, A. Stieger, D. Stenger, C. Scheuer, J. Holstein, T. Pohlemann, M. Menger, and T. Histing, “Comparison of Healing Process in Open Osteotomy Model and Open Fracture Model: Delayed Healing of Osteotomies after Intramedullary Screw Fixation,” *J. Orthop. Res.*, no. 2015.

[86] “Analysis of bone by micro-CT General information.” Bruker microCT, pp. 1–41.

[87] M. Bouxsein, S. Boyd, B. Christiansen, R. Guldberg, K. Jepsen, and R. Muller, “Guidelines for Assessment of Bone Microstructure in Rodents Using Micro-Computed Tomography,” *J. Bone Miner. Res.*, vol. 25, no. 7, pp. 1468–1486, 2010.

[88] M. Postek, “Scanning Electron Microscope,” in *Handbook of Charged Particle Optics*, J.

Orloff, Ed. New York: CRC Press, 1997.

[89] A. Boyde and S. Jones, “Scanning Electron Microscopy of Bone: Instrument, Specimen, and Issues,” *Microsc. Res. Tech.*, vol. 120, pp. 92–120, 1996.

[90] M. Morris and G. Mandair, “Raman assessment of bone quality,” *Clin. Orthop. Relat. Res.*, vol. 469, no. 8, pp. 2160–9, 2011.

[91] A. Merlen, V. Gadenne, J. Romann, V. Chevallier, L. Patrone, and J. Valmalette, “Surface enhanced Raman spectroscopy of organic molecules deposited on gold sputtered substrates,” *Nanotechnology*, vol. 20, p. 215705, 2009.

[92] D. William and C. Carter, *Transmission Electron Microscopy*. New York: Springer, 2009.

[93] R. Egerton, “Electron energy-loss spectroscopy in the TEM,” *Reports Prog. Phys.*, vol. 72, no. 1, p. 016502, 2008.

[94] “Transmission Electron Microscopy Analysis of Nanoparticles.” NanoComposix, California, pp. 2–3, 2012.

[95] “Sample Preparation Into Ultra-thin Sections.” St. Lawerence University, New York, pp. 1–24.

[96] N. Follak, I. Klöting, D. Ganzer, and H. Merk, “Scanning electron microscopic examinations on retarded bone defect healing in spontaneously diabetic BB/O(ttawa)K(arlsburg) rats,” *Histol. Histopathol.*, pp. 111–120, 2003.

[97] J. Gosman, Z. Hubbell, C. Shaw, and T. Ryan, “Development of Cortical Bone Geometry in the Human Femoral and Tibial Diaphysis,” *Anat. Rec.*, vol. 296, no. 5, pp. 774–787, 2013.

[98] R. Dubey, D. Gupta, and A. Singh, “Dental implant survival in diabetic patients; review

and recommendations," *National journal of maxillofacial surgery*, vol. 4, no. 2. pp. 142–50, 2013.

[99] G. Pavya and N. A. Babu, "Effect of Diabetes in Osseointegration of Dental Implant - A Review," *Biomed. Pharmacol. J.*, vol. 8, pp. 353–358, 2015.

[100] Y. Yeni, J. Yerramshetty, O. Akkus, C. Pechey, and C. Les, "Effect of Fixation and Embedding on Raman Spectroscopic Analysis of Bone Tissue," *Calcif. Tissue Int.*, pp. 363–371, 2006.

[101] G. Boivin, D. Farlay, Y. Bala, A. Doublier, P. Meunier, and P. Delmas, "Influence of remodeling on the mineralization of bone tissue," *Osteoporos. Int.*, vol. 20, no. 6, pp. 1023–1026, 2009.

[102] S. Schrof, P. Varga, L. Galvis, K. Raum, and A. Masic, "3D Raman mapping of the collagen fibril orientation in human osteonal lamellae," *J. Struct. Biol.*, vol. 187, no. 3, pp. 266–275, 2014.

[103] A. Carden, R. Rajachar, M. Morris, and D. Kohn, "Ultrastructural Changes Accompanying the Mechanical Deformation of Bone Tissue: A Raman Imaging Study," *Calcif. Tissue Int.*, vol. 72, no. 2, pp. 166–175, 2003.

[104] M. Schaeberle, H. Morris, J. Turner II, and P. Treado, "Raman Chemical Imaging Spectroscopy," *Anal. Chem.*, vol. 71, no. 5, pp. 175–181, 1999.

[105] M. Tzaphlidou and P. Berillis, "Collagen fibril diameter in relation to bone site. A quantitative ultrastructural study," *Micron*, vol. 36, no. 7–8, pp. 703–705, 2005.

[106] A. Roschger, P. Messmer, and P. Fratzl, "Relationship between the v2PO4⁄amide III ratio assessed by Raman spectroscopy and the calcium content measured by quantitative

backscattered electron microscopy in healthy human osteonal bone," *Biomed. Opt.*, 2013.

[107] N. Reznikov, R. Almany-Magal, R. Shahar, and S. Weiner, "Three-dimensional imaging of collagen fibril organization in rat circumferential lamellar bone using a dual beam electron microscope reveals ordered and disordered sub-lamellar structures," *Bone*, vol. 52, no. 2, pp. 676–83, 2013.

[108] E. Wolf, C. Braun-Reichhart, E. Streckel, and S. Renner, "Genetically engineered pig models for diabetes research," *Transgenic Res.*, vol. 23, no. 1, pp. 27–38, 2014.

[109] S. Milz and E. Schneider, "Animal Models for Implant Biomaterial Research in Bone : A Review," *Eur. Cells Mater.*, vol. 13, no. 0, pp. 1–10, 2007.

[110] C. Von Wilmowsky, P. Stockmann, I. Harsch, K. Amann, P. Metzler, R. Lutz, T. Moest, F. W. Neukam, and K. A. Schlegel, "Diabetes mellitus negatively affects peri-implant bone formation in the diabetic domestic pig," *J. Clin. Periodontol.*, vol. 38, no. 8, pp. 771–779, 2011.

APPENDIX A – COPYRIGHT PERMISSION

Copyright permission for the reproduction of figures in this thesis was granted from each journal.

The corresponding RightsLink permissions are included below.

Order Date	Article Title	Publication	Type Of Use	Order Status	Order Number
6-Sep-2016	Organization of apatite crystals in human woven bone	Bone	reuse in a thesis/dissertation	Completed	3943121215281
6-Sep-2016	Scanning electron microscopy: an introduction	III-Vs Review	reuse in a thesis/dissertation	Completed	3943130318279
6-Sep-2016	Nanoscale changes in collagen are reflected in physical and mechanical properties of bone at the microscale in diabetic rats	Bone	reuse in a thesis/dissertation	Completed	3943130600355
8-Sep-2016	Bioinspired structural materials	Nature Materials	reuse in a dissertation / thesis	Completed	3944250981725
8-Sep-2016	Mineral and Organic Matrix Interaction in Normally Calcifying Tendon Visualized in Three Dimensions by High-Voltage Electron Microscopic Tomography and Graphic Image Reconstruction	Journal of Structural Biology	reuse in a thesis/dissertation	Completed	3944290991798
8-Sep-2016	Organization of apatite crystals in human woven bone	Bone	reuse in a thesis/dissertation	Completed	3944300236400
8-Sep-2016	Dark-field transmission electron microscopy of cortical bone reveals details of extrafibrillar crystals	Journal of Structural Biology	reuse in a thesis/dissertation	Completed	3944301011877
8-Sep-2016	Bone structure and formation: A new perspective	Materials Science and Engineering: R: Reports	reuse in a thesis/dissertation	Completed	3944341302136